

A New Possible Accretion Scenario for Ultra-Luminous X-ray Sources

Shogo B. Kobayashi,^{1*} K. Nakazawa,² and K. Makishima^{3,4,5}

¹*Department of Physics, Tokyo University of Science, 1-3 Kagurazaka, Shinjuku-ku, Tokyo, 162-8601, Japan*

²*Division of Particle and Astrophysical Science, and Kobayashi-Maskawa Institute for the Origin of Particles and the Universe, Nagoya University, Furo-cho Chikusa-ku, Nagoya, 464-8602, Japan*

³*High Energy Astrophysics Laboratory, The Institute of Physics and Chemical Research (RIKEN), 2-1 Hirosawa, Wako, Saitama, 351-0198, Japan*

⁴*Department of Physics, The University of Tokyo, 7-3-1 Hongo, Bunkyo-ku, Tokyo, 113-0033, Japan*

⁵*Kavli Institute for the Physics and Mathematics of the Universe, The University of Tokyo, 5-1-5 Kashiwa-no-ha, Kashiwa, Chiba, 277-8683, Japan*

Accepted XXX. Received YYY; in original form ZZZ

ABSTRACT

Using archival data from *Suzaku*, *XMM-Newton*, and *NuSTAR*, nine representative Ultra-Luminous X-ray sources (ULXs) in nearby galaxies were studied. Their X-ray spectra were all reproduced with a multi-color disk emission model plus its Comptonization. However, the spectral shapes of individual sources changed systematically depending on the luminosity, and defined three typical spectral states. These states differ either in the ratio between the Comptonizing electron temperature and the innermost disk temperature, or in the product of Compton γ -parameter and fraction of the Comptonized disk photons. The luminosity range at which a particular state emerges was found to scatter by a factor of up to 16 among the eight ULXs. By further assuming that the spectral state is uniquely determined by the Eddington ratio, the sample ULXs are inferred to exhibit a similar scatter in their masses. This gives a model-independent support to the interpretation of ULXs in terms of relatively massive black holes. None of the spectra showed noticeable local structures. Especially, no Fe K-shell absorption/emission lines were detected, with upper limits of 30 – 40 eV in equivalent width from the brightest three among the sample; NGC 1313 X-1, Holmberg IX X-1, and IC 342 X-1. These properties disfavor ordinary mass accretion from a massive companion star, and suggest direct Bondi-Hoyle accretion from dense parts of the interstellar medium.

Key words: black hole physics – X-ray: binaries

1 INTRODUCTION

By the end of 2017 August, the gravitational wave telescopes LIGO and Virgo have so far detected 10 gravitational-wave events from merging black holes (BHs) (Abbott et al. 2016a,b; Abbott et al. 2017a; Abbott et al. 2017b; The LIGO Scientific Collaboration et al. 2018). Out of the 20 component BHs involved in these events, 15 have masses higher than $20 M_{\odot}$, where M_{\odot} is the solar mass. Furthermore, the 20 remnant BHs have a rather flat mass distribution from $18M_{\odot}$ to $80M_{\odot}$. Clearly, the mass range of these BHs is significantly higher than that of BHs in X-ray emitting BH binaries (BHBs), namely, 5 – 16 M_{\odot} (Özel et al. 2010), and that of theoretically predicted BHs (e.g., Belczynski et al.

2010) as an endpoint of massive stars (except Population III ones or those in a low metallicity environment). These newly recognized objects can potentially fill the gap in the BH mass distribution between $\sim 20M_{\odot}$ to $\sim 10^4M_{\odot}$. We are hence encouraged to search other astrophysical phenomena for similar “massive stellar BHs”, or intermediate-mass BHs (IMBHs).

One candidate for such BHs is extra-Galactic X-ray emitters called Ultra-Luminous X-ray Sources (ULXs), as initially suggested by Makishima et al. (2000). These are located on the arms of spiral galaxies (Fabbiano & Trinchieri 1987), and their luminosities, $L_X = 10^{39-41}$ erg sec⁻¹, often exceed significantly the Eddington luminosity L_{edd} of stellar mass ($\sim 10 M_{\odot}$) BHs. Supposing that ULXs are emitting X-rays in the sub-Eddington regime, they are expected to harbor the missing intermediate-mass BHs as their cen-

* E-mail: shogo.kobayashi@rs.tus.ac.jp

tral objects (Makishima et al. 2000). However, their X-ray spectra appear different from what are observed from Galactic/Magellanic BH binaries. This fact, together with yet unknown scenario of the formation of BHs in such a mass range, led many authors to consider alternative interpretations, such as emission from stellar mass BHs that are accreting at super-critical rates (e.g., Mineshige & Ohsuga 2007; Kawashima et al. 2012), possibly with highly anisotropic radiation beamed toward us (e.g., King et al. 2001). Since the sources are extra Galactic, their mass donating companions have not been firmly identified except several cases (Motch et al. 2014; Heida et al. 2015), and hence little constraints have been obtained on the dynamical mass of their central objects.

In 2014, the ~ 1.4 sec coherent hard X-ray pulsation was detected with *NuSTAR* from a central region of the starburst galaxy M82 (Bachetti et al. 2014), and its source was identified by *Chandra* as the ULX known as M82 X-2. After this epoch-making discovery, some authors (Fürst et al. 2016; Israel et al. 2017a,b; Carpano et al. 2018) searched the archival X-ray data of ULXs for similar pulsations, and detected three more examples; NGC 7793 P-13 with a period of ~ 0.4 sec, NGC 5907 X-1 with ~ 1.3 sec, and NGC 300 ULX-1 with ~ 32 sec. These results have demonstrated that some ULXs do contain neutron stars (NSs) as their compact components, which are apparently radiating (if isotropic) at ~ 100 times the Eddington luminosity for a typical $1.4 M_{\odot}$ NS. Although these “NS ULXs” impose a new challenge to our understanding of ULXs, they tend to exhibit spectra with higher cutoff energies and/or harder continua than those of the others (Brightman et al. 2016; Pintore et al. 2017). Therefore, we still regard the remaining majority of ULXs as accreting BHs, and use the term “ULX” without including the NS ULXs.

Since observational information on ULXs is limited in other wavelengths, their X-ray spectra still provide major clues to their nature. As the luminosity changes, ULXs are considered to take three different spectral states with characteristic continuum shapes (Gladstone et al. 2009; Miyawaki et al. 2009; Sutton et al. 2013). One is so-called the Soft Power Law (SPL) state, wherein the spectrum exhibits a low energy hump at ~ 1 keV, on top of a soft Power Law (PL) component with a photon index of $\Gamma \sim 2.4$ and a high-energy roll over at ~ 5 keV. As the source brightens, it moves into a second state called the Hard PL (HPL) state, in which the PL continuum becomes literally harder ($\Gamma \sim 1.7$) and shows a slightly higher cutoff energy (~ 8 keV) than in the SPL state. Finally, when the source brightens even further, the soft excess becomes less visible and the cutoff energy decreases, and the overall spectrum takes a convex shape; this is called the Multi-Color Disk like (MCD) state.

These kinds of spectral transition phenomena are widely observed in other accreting compact objects, including black-hole binaries (BHBs; e.g., Remillard & McClintock 2006), low-mass X-ray binaries involving weakly magnetized NSs (e.g., Sakurai et al. 2014), and Seyfert galaxies as recently revealed by Noda et al. (2014). In all these cases, the spectral states are approximately specified by the Eddington ratio $\eta \equiv L_X/L_{\text{edd}}$, where L_X is the X-ray luminosity. If this basic property of accreting systems also applies to ULXs, we are able to estimate how widely their masses are

distributed, just by studying the scatter of state-transition threshold luminosities among ULXs.

While ULX spectra exhibit the various types of spectral continua as described above, they show little local features in their spectra such as emission/absorption lines or absorption edges. Especially, the features from Fe K-shell, which are ubiquitously seen in other accreting objects, are absent or very weak in their spectra. Although some authors succeeded to detect several resonance line features of Ne, O, and Fe from a few ULXs, these features are as weak as a few eV in equivalent width (Pinto et al. 2016; Walton et al. 2016). Generally, these local features are considered to reflect the surrounding environment, including the geometry, density, velocity, and the ionization states of the accreting matters. Therefore, the absence or weakness of these features suggest some difference of ULXs from the other types of accreting objects in their accretion scheme.

In the present paper, we analyze archival data of several representative ULX sources, and study the distribution of their state emerging luminosities by tracking their mid-term (~ 10 ks) to long-term ($>$ days) variability. We also search their spectra for local features from Fe K-shell. Based on these observational results, a novel accretion scheme is proposed to explain the basic properties of ULXs.

2 OBSERVATIONS AND DATA REDUCTIONS

We utilized archive data obtained with *XMM-Newton*, *Suzaku*, and *NuSTAR*. To discriminate ULXs from less exotic accreting systems (including ordinary stellar-mass BHs), we limited our studies to those of which the observed maximum luminosity exceeds L_{edd} of the heaviest class of stellar-mass BHs in our galaxy ($\sim 15 M_{\odot}$), namely, $\sim 2 \times 10^{39}$ erg sec $^{-1}$. In addition, to acquire sufficient photon statistics, the targets were limited to those in nearby galaxies with a distance of ≤ 5 Mpc. Then, a typical ULX with $L_X \sim 2 \times 10^{39}$ erg sec $^{-1}$ will yield a few thousand photons to these X-ray observatories in a typical exposure of several tens ksec. Finally, to study spectral variability, we further limited our sample objects to those which were observed more than twice with either of the three observatories. As a result, nine ULXs as listed in table 1 have been selected. Table 2 summarizes basic information of the data sets we analyze in the present study.

2.1 *Suzaku* data

The *Suzaku* satellite (Mitsuda et al. 2007) is capable of broad band spectroscopy, by combining the X-ray Imaging Spectrometer (XIS; Koyama et al. 2007) operating in the 0.3–12 keV band, and the Hard X-ray Detector (HXD; Takahashi et al. 2007) in 15–600 keV. However, we utilize only the XIS data, since those of the HXD, being a non-imaging instrument, are often contaminated by emission from other X-ray sources. Because one of the four XIS cameras lost its function since 2006, we utilized the remaining two front illuminated (FI) type CCD cameras (XIS0, XIS3) and one back illuminated (BI) type one (XIS1). In spectral analysis, we excluded the 1.5–2.0 keV band to avoid calibration uncertainties therein, and co-added data from the two FI-XIS cameras because they have nearly identical responses.

Table 1. Summary of the ULXs studied in the present paper.

host galaxy	$N_{\text{H}}^{\text{Gal}a}$ ($\times 10^{20} \text{ cm}^{-2}$)	distance ^b (Mpc)	source name
M33	4.4	0.88	X-8
Holmberg II	3.9	3.3	X-1
IC 342	34.5	3.3	X-1
Holmberg IX	4.3	3.4	X-1
NGC 4190	2.1	3.5	X-1
NGC 1313	3.6	4.13	X-1
			X-2
M83	3.8	4.61	ULX-1
			ULX-2

Notes:^aGalactic equivalent hydrogen column densities toward each source, taken from [Dickey & Lockman \(1990\)](#). ^bDistances toward the host galaxies taken from NASA/IPAC Extragalactic Database.

To minimize the background, we discarded the data taken during and within 436 sec after exiting the South Atlantic Anomaly, and when the spacecraft was in the region where the cut off rigidity is less than 6 GV. Furthermore, to avoid strong solar X-ray albedo from the Earth’s atmosphere, we set the satellite elevation to be higher than 20° from the sunlit Earth. Incorporating these data screenings, the data reduction was carried out using the latest calibration database files and the `aepipeline` software, which is included in High Energy Astronomy SOFT (HEASOFT).

Each ULX spectrum was accumulated over a circular region with a radius of 2′.5, which corresponds to ~ 90% of the encircled energy function of the X-ray Telescope. Background spectra were extracted from circular or annular regions wherein no apparent X-ray source is present. In order to maximize the signal-to-noise ratio, the background accumulation region was set to be relatively large, with a radius up to 2′.

2.2 XMM-Newton data

The *XMM-Newton* observatory ([Barré et al. 1999](#)) allows high-sensitivity observations in 0.3 – 10 keV with the European Photon Imaging Cameras (EPIC), which consists of two Metal-Oxide Semiconductor type CCD detectors (MOS; [Turner et al. 2001](#)), and a pn junction type one (PN; [Strüder et al. 2001](#)).

The gain calibrations and removal of bad quality events for MOS and PN were carried out with `emchain` and `epchain`, respectively, both included in the Science Analysis System package. In addition, solar flare proton events were also removed by referring to light curves above 10 keV, where the X-ray mirror has nearly zero reflectivity. We discarded events taken in the time intervals where the count rate is twice as high as the average. We created the MOS-1 and MOS-2 spectra separately, and fitted them simultaneously.

Considering the angular resolution of *XMM-Newton* (~ 15″ in half power diameter), we extracted spectra of the target ULXs from circular regions with a radius of 30″, which encircles typically 83–88% of the source photons. The background spectra were taken from the same observation as

the on-source spectra, but from a region wherein no apparent X-ray sources are detected. To avoid known positional dependence, we further limited the background region to be within the CCD chip in which the target source is present. As a result, the background region generally became a circle with a radius of 30″ – 45″ and 30″ – 60″ for PN and MOS, respectively.

2.3 NuSTAR data

The *NuSTAR* satellite ([Harrison et al. 2013](#)) is capable of imaging spectroscopy in the 3 – 80 keV band, with two CdZnTe detector modules called Focal Plane Modules A and B, to be abbreviated as FPM-A and FPM-B, respectively ([Kitaguchi et al. 2014](#)). In the present paper, we utilize *NuSTAR* data for spectroscopic studies of ULXs in a broader energy band than those of the other satellites.

For the same reason as in *Suzaku*, we discarded the data taken during the South Atlantic Anomaly, or when the Earth was in the field of view, or when the elevation angle of the telescope above the Earth’s limb was less than 3°. We also excluded the data taken when the source made an excursion by > 6′ from the nominal position due to wobbles of the optical bench. All these data reductions and other calibrations were performed with the software tools, `nupipeline` and `nuproducts`, included in HEASOFT.

The spectra of ULXs were extracted from circular regions of 30″ radius, while those of background from regions with a radius of 2′. Since a single FPM module consists of four CdZnTe detector chips, we defined the background region in the same chip as the target source, for the same reason as in *XMM-Newton*. Just like the EPIC data, we created the FPMA and FPMB spectra separately, and fitted them simultaneously.

3 DATA ANALYSIS AND RESULTS

3.1 Light Curves

In figure 1, we present background subtracted 0.3 – 10 keV light curves obtained from three representative observations in our sample; that of Holmberg IX X-1, IC342 X-1, and NGC 1313 X-1. As seen in the first two sources, typical X-ray intensity variations of the sample ULXs were no more than 30% within each observation. Hence, we basically derived a single averaged spectrum from each data set. However, as in figure 1 c, NGC 1313 X-1 varied, on 2014 May 27, by a factor of ~ 2 (in 0.5–10 keV) on a time scale of several ks. We hence divided this particular data set into three intensity intervals, low (< 0.65 counts sec⁻¹), middle (0.65 – 0.85 counts sec⁻¹), and high (> 0.85 counts sec⁻¹), and made a spectrum from each of them.

3.2 Continuum Spectroscopy

3.2.1 The model fitting

The obtained spectra are presented in figures 2 and 3, after subtracting the background and using the νF_{ν} form where the instrumental responses are approximately removed. Thus, most of the sources exhibited significant

Table 2. Observational log.

Host galaxy	ObsID ^a	RA ^b (deg)	Dec ^c (deg)	Observation Start yyyy/mm/dd hh:mm:ss	Exposure ^d (ks)	Observatory
NGC 1313	0150280301	49.66304	-66.59972	2003/12/21 01:54:45	7.4	<i>XMM-Newton</i>
	0150280401	49.66196	-66.60047	2003/12/23 04:50:43	10.6	<i>XMM-Newton</i>
	0150280601	49.65758	-66.60817	2004/01/08 03:30:34	6.0	<i>XMM-Newton</i>
	0150281101	49.65250	-66.61319	2004/01/16 23:38:52	6.3	<i>XMM-Newton</i>
	0205230301	49.5170	-66.60464	2004/06/05 06:08:51	8.5	<i>XMM-Newton</i>
	0205230401	49.55733	-66.57292	2004/08/23 05:44:43	11.1	<i>XMM-Newton</i>
	0205230501	49.65583	-66.58697	2004/11/23 06:59:33	12.3	<i>XMM-Newton</i>
	0205230601	49.63488	-66.62122	2005/02/07 11:35:10	7.7	<i>XMM-Newton</i>
	100032010	49.5282	-66.5443	2005/10/15 13:21:13	32.9	<i>Suzaku</i>
	0301860101	49.42263	-66.57953	2006/03/06 16:43:12	16.7	<i>XMM-Newton</i>
	0405090101	49.59296	-66.47497	2006/10/15 23:44:33	69.4	<i>XMM-Newton</i>
	703010010	49.6088	-66.5434	2008/12/05 23:03:23	91.5	<i>Suzaku</i>
	30002035002	49.6268	-66.5225	2012/12/16 13:56:07	100.8	<i>NuSTAR</i>
	0693850501 [†]	49.63108	-66.49931	2012/12/16 16:00:25	92.1	<i>XMM-Newton</i>
	30002035004	49.6351	-66.5268	2012/12/21 20:06:07	127.0	<i>NuSTAR</i>
	0693851201 [†]	49.63305	-66.50272	2012/12/22 15:45:31	80.8	<i>XMM-Newton</i>
	0722650101	49.33767	-66.55542	2013/06/08 05:21:44	11.3	<i>XMM-Newton</i>
	709023010	49.4840	-66.5362	2014/05/27 05:41:09	107.3	<i>Suzaku</i>
	Holmberg IX	0111800101	148.89925	69.03797	2001/04/22 10:20:33	7.6
0112521001		149.46213	69.03264	2002/04/10 16:58:14	7.0	<i>XMM-Newton</i>
0112521101		149.46804	69.03222	2002/04/16 17:33:15	7.4	<i>XMM-Newton</i>
0200980101		149.50104	69.09072	2004/09/26 07:25:12	56.9	<i>XMM-Newton</i>
0657801801		149.21079	69.09094	2011/09/26 04:17:58	11.9	<i>XMM-Newton</i>
0693850801 [†]		149.47125	69.09203	2012/10/23 04:17:03	8.8	<i>XMM-Newton</i>
0693851001 [†]		149.46817	69.09231	2012/10/27 04:04:42	3.3	<i>XMM-Newton</i>
30002033006		151.1143	68.5532	2012/11/11 16:51:07	35.2	<i>NuSTAR</i>
0693851701 [†]		149.44925	69.09156	2012/11/12 03:04:01	7.1	<i>XMM-Newton</i>
30002033008		151.1297	68.5537	2012/11/14 01:31:07	14.5	<i>NuSTAR</i>
0693851801 [†]		149.44767	69.09117	2012/11/14 02:55:07	6.3	<i>XMM-Newton</i>
30002033010		151.1297	68.5537	2012/11/15 17:51:07	49.0	<i>NuSTAR</i>
0693851101 [†]		149.44658	69.09083	2012/11/16 02:52:38	2.7	<i>XMM-Newton</i>
Holmberg II		0112520601	124.8950	70.67828	2002/04/10 12:31:19	4.6
	0112520701	124.90204	70.67975	2002/04/16 12:06:26	3.9	<i>XMM-Newton</i>
	0112520901	124.8760	70.73356	2002/09/18 02:10:13	4.4	<i>XMM-Newton</i>
	0200470101	124.90079	70.67844	2004/04/15 20:08:43	33.8	<i>XMM-Newton</i>
	0561580401	124.87692	70.67714	2010/03/26 09:20:48	21.8	<i>XMM-Newton</i>
	30001031002	124.8517	70.684	2013/09/09 05:41:07	31.3	<i>NuSTAR</i>
	0724810101 [†]	124.88775	70.73364	2013/09/09 06:33:44	4.4	<i>XMM-Newton</i>
	30001031003	124.9776	70.693	2013/09/09 17:31:07	79.4	<i>NuSTAR</i>
	30001031005	124.9655	70.7048	2013/09/17 04:46:07	111.1	<i>NuSTAR</i>
	0724810301 [†]	124.87921	70.73342	2013/09/17 06:03:28	4.9	<i>XMM-Newton</i>
IC 342	0206890101	56.57808	68.11403	2004/02/20 06:30:24	17.3	<i>XMM-Newton</i>
	0206890201	56.47533	68.15733	2004/08/17 18:48:16	17.1	<i>XMM-Newton</i>
	0206890401	56.57175	68.11256	2005/02/10 17:26:36	6.3	<i>XMM-Newton</i>
	30002032002	58.4077	67.7677	2012/08/10 08:21:07	21.0	<i>NuSTAR</i>
	0693850601 [†]	56.43046	68.10256	2012/08/11 20:06:44	35.5	<i>XMM-Newton</i>
	30002032005	58.4635	67.844	2012/08/16 08:26:07	127.4	<i>NuSTAR</i>
0693851301 [†]	56.43146	68.10375	2012/08/17 19:48:41	32.4	<i>XMM-Newton</i>	
M83	0723450101	204.2760	-29.89686	2013/08/07 16:38:29	44.7	<i>XMM-Newton</i>
	0723450201	204.26263	-29.84075	2014/01/11 11:59:44	37.5	<i>XMM-Newton</i>
	0729561201	204.28029	-29.89628	2014/07/06 17:45:59	24.0	<i>XMM-Newton</i>
	0729561001	204.26696	-29.84067	2015/02/02 16:00:02	14.3	<i>XMM-Newton</i>
NGC 4190	0654650101	183.44208	36.60292	2010/06/06 12:08:27	1.9	<i>XMM-Newton</i>
	0654650201	183.44233	36.60336	2010/06/08 11:14:45	8.5	<i>XMM-Newton</i>
	0654650301	183.43221	36.65992	2010/11/25 01:24:51	11.2	<i>XMM-Newton</i>

Notes: [†]Observations that are combined with *NuSTAR*. ^aObservational ID numbers of the data sets. ^bRight-ascensions of the aim points. ^cDeclination of the telescope aim points. ^dExposure time after the reduction of the SAA-passage/proton-flare intervals.

Table 2 – *continued*

Host galaxy	ObsID ^a	RA ^b (deg)	Dec ^c (deg)	Observation Start yyyy/mm/dd hh:mm:ss	Exposure ^d (ks)	Observatory
M33	0102640101	23.43317	30.67694	2000/08/04 05:17:12	5.3	<i>XMM-Newton</i>
	0102640301	23.35442	30.88608	2000/08/07 01:03:49	3.5	<i>XMM-Newton</i>
	0141980801	23.49225	30.64731	2003/02/12 15:17:46	6.8	<i>XMM-Newton</i>
	704016010	23.4896	30.5679	2010/01/11 01:47:07	82.5	<i>Suzaku</i>

Notes: [†]Observations that are combined with *NuSTAR*. ^aObservational ID numbers of the data sets. ^bRight-ascensions of the aim points. ^cDeclination of the telescope aim points. ^dExposure time after the reduction of the SAA-passage/proton-flare intervals.

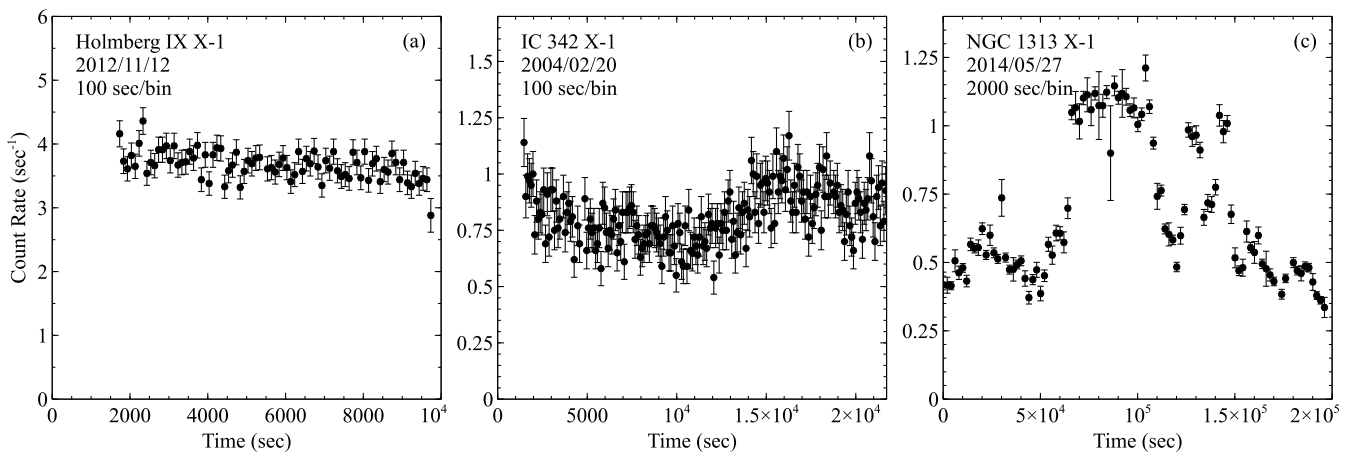


Figure 1. Examples of 0.3 – 10 keV background-subtracted light curves of the objects in the present sample. The source name and the observing epoch are indicated at the top of each panel. The data in (a) and (b) were taken with EPIC-PN, while that of (c) with XIS0+XIS3. They are uncorrected for the vignetting effect. The zero second of each light curve is set to the start point of its observation. All events taken during high background rates (e.g., soft proton flares) were excluded.

changes in their spectral shapes over the observational history spanning ~ 10 years. In many of them, the variation is more pronounced in > 1 keV than in < 1 keV. Some sources, including NGC 1313 X-1, Holmberg IX X-1, IC 342 X-1, and M83 ULXs, showed series of convex spectra which are typical of the MCD state. As they became dimmer, the spectrum started showing the hard PL continua and soft excess components at ~ 1 keV, which are typical characteristics of the HPL state. Furthermore, in NGC 1313 X-1 and Holmberg II X-1, the PL slope softened to $\Gamma > 2.0$ and the soft excess became more prominent as the luminosity decreased; the spectra finally reached the SPL state. This behavior is consistent with that found, e.g., by Gladstone et al. (2009), Sutton et al. (2013).

To quantify the shapes of the sample spectra, we fitted them with a model commonly used in studies of accreting BH systems; it consists of a multi-color disk model and its thermal Comptonization (MCD+THC modeling; Makishima et al. 2008). In the modeling, we assume that a standard accretion disk (Shakura & Sunyaev 1973) is partially covered by a hot electron cloud, which Compton up-scatters some fraction of the photons from the disk (Gladstone et al. 2009). The remaining disk photons are assumed to reach the observer as the direct MCD component. According to Gladstone et al. (2009), this model can describe the three spectral states in a unified way, and provide reasonable physical in-

terpretations. We retain the two components even if either of them is not strongly required by the data, because its upper limit is still meaningful.

Although the MCD+THC modeling is widely used to fit spectra in the HPL and SPL states, those in the MCD state, with convex shapes and high luminosity, are often explained with an alternative accretion disk model called “slim disk”. This is an accretion-flow solution expected to emerge near or above the Eddington rate (Abramowicz et al. 1988; Watarai et al. 2000), and characterized by a flatter radial temperature gradient than the standard disk. A slim-disk spectrum is often approximated analytically with a “free- p disk” model, which is a modified MCD model with the temperature gradient index p set free, instead of being fixed at $p = 0.75$ as in a standard disk. In fact, the slim disk model reproduces the same MCD state spectra as successfully as the MCD+THC modeling (e.g., Miyawaki et al. 2009; Middleton et al. 2011; Bachetti et al. 2013), usually without significant statistical differences. However, Miyawaki et al. (2009) have showed that the slim-disk interpretation of the spectrum of M82 X-1 in the MCD state leads to some physical inconsistency, including too high a disk temperature. Furthermore, the model also fails to give a consistent explanation to the spectral variability of several ULXs (e.g., Mizuno et al. 2007). For these reasons, we employ the MCD+THC modeling throughout the present work.

Using the above model, we analyze background-subtracted spectra of the sample ULXs with the HEASOFT XSPEC analysis software, employing the chi-squared statistics. Prior to the fitting, the background-subtracted spectra were re-binned, so that each energy bin has $\gtrsim 20$ counts. Although the *NuSTAR* FPM is capable of detecting X-rays up to ~ 80 keV, the curving spectral shapes and rebinning criteria (typically $\delta E/E \sim 0.1$ and $\gtrsim 5$ in signal-to-noise ratio) allowed us to detect the sources only up to ~ 15 keV. The `diskbb` model (Mitsuda et al. 1984; Makishima et al. 1986) and the `nthcomp` model (Zdziarski et al. 1996; Życki et al. 1999) were employed to express the direct MCD and the THC components, respectively. The former has the innermost disk radius R_{raw} and the temperature T_{in} as free parameters. The latter is specified by the photon index Γ describing the continuum slope, and the electron temperature T_e characterizing the high-energy bend. The seed photon temperature of `nthcomp` is set to be identical to T_{in} . Assuming that the photon number is conserved in Compton scattering, we can convert the `nthcomp` flux to the linear size of the disk, R_{thc} , that is covered with the corona. The conversion is made by calculating a `diskbb` model that gives the same temperature and photon flux as the `nthcomp` component. Accordingly, the innermost radius of the whole accretion disk R_{tot} can be calculated as

$$R_{\text{tot}}^2 = R_{\text{raw}}^2 + R_{\text{thc}}^2 \quad (1)$$

(e.g., Kubota & Makishima 2004, Makishima et al. 2008).

The photoelectric absorption was taken into account by applying two `tbabs` (Wilms et al. 2000) factors to the constructed model, one representing the Galactic line-of sight absorption and the other that from the host galaxy (including circum-source contributions). The equivalent hydrogen column density N_{H}^G of the former was fixed at the values by Dickey & Lockman (1990), whereas that of the latter, to be denoted as N_{H} , was left free. An exception is NGC 1313 X-1, where we replaced the second `tbabs` to the `vphabs` model, which allows us to freely change the abundances of individual elements. This is because the source is possibly residing in an oxygen-poor environment (Mizuno et al. 2007); following Mizuno et al. (2007), we fixed the abundance of oxygen to 0.68 times the solar value, while the others at the solar abundance.

Finally, we multiplied an additional constant factor to the model, to deal with systematic relative uncertainties in the absolute photoelectric sensitivity among different types of detectors. This parameter was allowed to vary freely when the spectral analysis involve different instruments; otherwise, it was frozen to unity.

Table 3 summarizes the best-fit parameters and the fit goodness, obtained through the spectral fitting analysis described above. Here and hereafter, all the errors refer to 90% confidence level unless stated otherwise. Although most of the sources showed the strong variability in their spectral shapes, the MCD+THC model has successfully reproduced most of the spectra, as shown by solid lines in figures 2 and 3. In agreement with the low variability below 1 keV, N_{H} was relatively stable, and rather low as $N_{\text{H}} \sim 10^{21} \text{ cm}^{-2}$ or even less in some sources (e.g., M83 ULX-1 and ULX-2). For example, the X-ray luminosity of NGC 1313 X-1 changed nearly by an order of magnitude, but the error-

weighted mean and the standard deviation of the column density was $N_{\text{H}} = (2.1 \pm 0.9) \times 10^{21} \text{ cm}^{-2}$.

Due to the characteristic spectral bend at 5–7 keV, all sources required rather low electron temperatures as $T_e = 0.9 - 2.0$ keV, except data with insufficient statistics in the 7–10 keV band. The derived photon index is distributed over a rather wide range of $\Gamma = 1.6 - 2.7$, reflecting the large spectral shape changes above 2 keV. Since Γ represents the Compton y -parameter as $y = 4/[(0.5 + \Gamma)^2 - 2.5]$, we can obtain the optical depth of the corona, τ , by combing Γ and T_e as

$$\tau = \left[2.25 + \frac{3}{(T_e/511 \text{ keV})[(\Gamma + 0.5)^2 - 2.25]} \right]^{0.5} - \frac{3}{2} \quad (2)$$

(Sunyaev & Titarchuk 1980). This equation generally yields $\tau \sim 5 - 19$ for the present sample (table 3). Since τ depends on the two parameters, T_e and Γ , which are correlated with each other, the statistical uncertainty of τ was calculated by taking the covariance between them.

Although the MCD+THC model has been generally successful, a few spectra of NGC 1313 X-1 gave slightly worse fits as $\chi^2/\nu = 1.25 - 1.35$. These are all caused by two types of local features seen in residuals below 1 keV. One is the residuals at 0.56 keV (e.g., figure 2 panels A and B) which is likely to be neutral Oxygen K-edge absorption feature caused by inaccurate estimates of the Oxygen abundance of local absorbers around NGC 1313 X-1. In fact, the residual disappears if we let the Oxygen abundance in `vphabs` increase to 0.71 times solar, from the tentatively assumed value of 0.68. The other is an unaccounted positive structure at ~ 1 keV (e.g., figure 2 panel C). Similar local residuals are also reported in other ULXs (e.g., NGC 5408 X-1; Middleton et al. 2014), and their origin is still under a debate. Further examination of the ~ 1 keV residuals is beyond the scope of the present paper, because our major objective is to quantify the continuum.

3.2.2 Spectral state characterization

Now that the MCD+THC modeling has thus been successful, next we try to characterize the individual spectral states in terms of the obtained model parameters. For example, as shown by figure 3 (A) and (B), Holmberg IX X-1 exhibited two distinct types of spectral states, to be identified with the HPL state and the MCD state. As the source brightened, the spectrum changed gradually in shape from two-humped ones (figure 3 panel B) typical of the former state, to more convex ones (figure 3 panel A) often seen in the latter state. In terms of the spectral fit parameters, this spectral change, or transition, from the HPL to MCD states as the luminosity increases, can be characterized by two effects. One is mutual approach between T_{in} and T_e , because T_{in} increased from ~ 0.3 keV to 0.6–0.9 keV, whereas T_e decreased slightly from 2.6 keV to 1.6–2.0 keV. The other is a marked decrease of R_{raw} , or the directly visible disk fraction, because the soft excess becomes no longer visible in the convex-shaped MCD state.

Spectral transitions of the same type as that of Holmberg IX X-1 were also seen in other five sources, NGC 1313 X-1, IC 342 X-1, M83 ULX-1, M83 ULX-2, and NGC 4190 X-1 (see figures 2 and 3). Most of them also showed increasing T_{in} , decreasing R_{raw} , and decreasing or comparable T_e

through their transitions from the HPL states to the MCD states. As an exception, several data sets of NGC 1313 X-1 and IC 342 X-1 in the MCD state showed rather lower temperatures as $T_{\text{in}} = 0.13 - 0.2$ keV and extremely large radii as $R_{\text{raw}} = 15000 - 17000$ km, despite their convex shaped spectra which are similar to those of the others. This is rather unphysical, because the results would imply that extremely large disks are present in the MCD states, and most of their emission is hidden below the detectable energy band. Therefore, we applied a slight modification to our modeling, as detailed in Appendix, assuming that the corona covers only a limited inner region of the disk. As shown in table 3, the alternative model gave similarly good fit as the original model, or even slightly better. The innermost temperature of the corona-covered disk region, $T_{\text{in}2} = 0.6 - 0.9$ keV, is consistent with the results obtained in the previous study (Kobayashi et al. 2016), and is higher than that in the HPL state (~ 0.2 keV). Thus, in these two sources, the transitions from the HPL state to the MCD state are also successfully explained by a decrease in the T_e/T_{in} ratio, and an increase of the covering fraction of the corona above the accretion disk.

While most of the sources resided either in the HPL or the MCD states, Holmberg II X-1 and NGC 1313 X-1 occasionally exhibited, in addition to the HPL spectra, those with even softer ($\Gamma > 2.0$) continuum, which is typical of the SPL state. This state assignment agrees with previous observations (e.g., Feng & Kaaret 2006; Kajava & Poutanen 2009; Kajava et al. 2012). The spectrum of Holmberg II X-1 obtained on 2002 September 18 (shown in green in figure 3 panel D) exhibits a strong hump with $T_{\text{in}} = 0.16 \pm 0.06$ keV and a soft $\Gamma > 2.6$ PL continuum with the lowest coronal temperature of $T_e = 0.8^{+1.0}_{-0.3}$ keV. As the source became more luminous, the spectrum made a transition toward the HPL state; the PL continuum hardened to $\Gamma = 1.8$ and T_e increased to ~ 2.4 keV, while T_{in} remained nearly unchanged at ~ 0.2 keV. Thus, the evolution from the SPL to the HPL state can be characterized not only by a hardening of the continuum, but also by an increase of the difference between T_{in} and T_e .

The only SPL-state data set from NGC 1313 X-1 (2004 August 23; figure 2 panel D) also showed the lowest electron temperature of $T_e = 0.9^{+0.6}_{-0.2}$, and a strong soft excess which can be reproduced by a disk with $T_{\text{in}} = 0.22 \pm 0.05$ keV. Just like the case of Holmberg II X-1, T_e significantly increased up to ~ 2.6 keV as the source brightened and made a transition to the HPL states, while T_{in} were nearly constant at 0.2 keV. Thus, both NGC 1313 X-1 and Holmberg II X-1 showed an increase in the T_e/T_{in} ratio through their transitions from the SPL state to the HPL state, while T_{in} remained nearly unchanged.

In contrast to the above seven sources, the remaining two, M33 X-8 and NGC 1313 X-2, exhibited the convex MCD state spectra throughout all epochs (figure 3 panels F and H). Both sources yielded rather high T_{in} as 0.21–0.53 keV and low T_e as 1.1–2.2 keV, compared to those seen in the HPL states of the other sources. In addition, the directly visible disk component was hardly required because these convex spectra were individually reproduced almost solely by an `nthcomp` model with a high T_{in} and low T_e . These characteristics in the derived parameters are consistent with

those in the MCD states of the other sources described so far.

3.3 Search for Fe-K line features

As described in section 3.5, the MCD+THC model successfully explained all the sample spectra, and none of them exhibited noticeable emission/absorption line features (except those of < 1 keV; section 3.2.1), including in particular Fe-K lines which are widely seen in X-ray spectra of various classes of accreting objects. Although the ULX spectra in our sample are thus generally featureless, each individual spectrum could still be insufficient in statistics to derive meaningful constraints on the Fe-K line features. Therefore, we have decided to co-add (stack) the separate spectra of each source into a single one, and search it for weak Fe-K lines under improved statistics.

Since the analysis requires high photon flux around the Fe-K edge energy (7.11 keV), we selected for this purpose three sources, NGC 1313 X-1, IC 342 X-1, and Holmberg IX X-1, which exhibited hard spectra with $\Gamma \sim 1.7$ and the highest X-ray flux ($> 10^{-11}$ erg sec $^{-1}$ cm $^{-2}$) among our sample. To avoid the obvious complication of adding up the data from different instruments, we limit the stacking analysis to the *XMM-Newton* data which are rather abundant, and utilize only those of EPIC PN which has a larger effective area than EPIC MOS at ~ 7 keV.

The top panels of figure 4 show the stacked PN spectra of the three sources, NGC 1313 X-1, Holmberg IX X-1, and IC 342 X-1, with a total exposure of 394 ks (14 spectra), 132 ks (11 spectra), and 113 ks (6 spectra), respectively. Since our interest is in Fe-K lines, we restricted the analyzing energy band to 4.0–8.5 keV, which is still wide enough to allow blue/red shifts up to 20% of the speed of light.

To quantify the continuum in this energy band, we fitted each stacked spectrum with a cutoff-PL model, as represented by the solid line superposed on the spectrum. This has already given a good fit with $\chi^2/\nu = 133.0/116$, $\chi^2/\nu = 80.34/86$, and $\chi^2/\nu = 87.7/96$, in NGC 1313 X-1, Holmberg IX X-1, and IC 342 X-1, respectively, where ν is the degree of freedom. In the fit residuals, we do not see noticeable emission/absorption features, except a possible dip at ~ 8 keV in NGC 1313 X-1, which is likely to have arisen from an over subtraction of the instrumental Cu-K line in the background spectrum.

To derive upper limits on the emission/absorption features, to the model we added a Gaussian with a width of 10 eV at various energies, allowed its normalization to take either positive or negative values, and scanned the energy with a step of 10 eV to calculate 99%-confidence upper limits on the allowed line equivalent width (EW). The results are given in light-blue strips in the bottom panels of figure 4. Thus, the stacked spectra have provided rather stringent limits on emission or absorption line features. Especially, around the energy where the Fe-K features without blue/red shifts are expected (red dashed lines in figure 4), we obtained 99% upper limits on the EW as 30 eV in NGC 1313 X-1, 35 eV in Holmberg IX X-1, and 55 eV in IC 342 X-1.

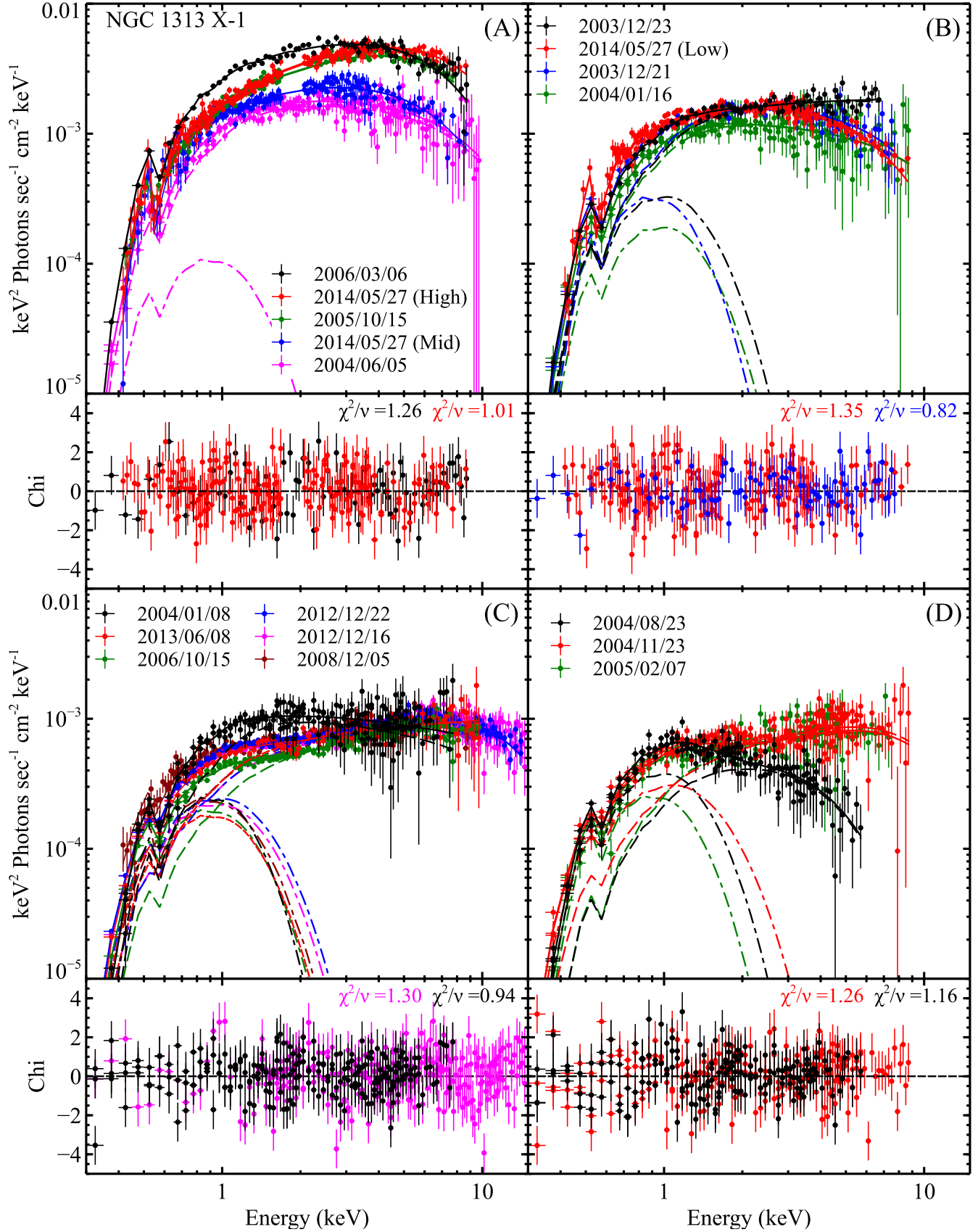


Figure 2. Spectra of NGC 1313 X-1 unfolded with the best fit MCD+THC models (solid lines). The dot-dashed lines represent the MCD component, while the dashed ones are the THC component. They are grouped into four in terms of their 0.3 – 10 keV luminosity. (A): $L_X > 1.3 \times 10^{40}$ erg sec $^{-1}$. (B): 8×10^{39} erg sec $^{-1} < L_X < 1.3 \times 10^{40}$ erg sec $^{-1}$. (C): 5×10^{39} erg sec $^{-1} < L_X < 8 \times 10^{39}$ erg sec $^{-1}$. (D): $L_X < 6.4 \times 10^{39}$ erg sec $^{-1}$. Each elongated panel presented at the bottom shows the residuals and reduced chi-squared values obtained from the best/worst fit results in the respective spectral group.

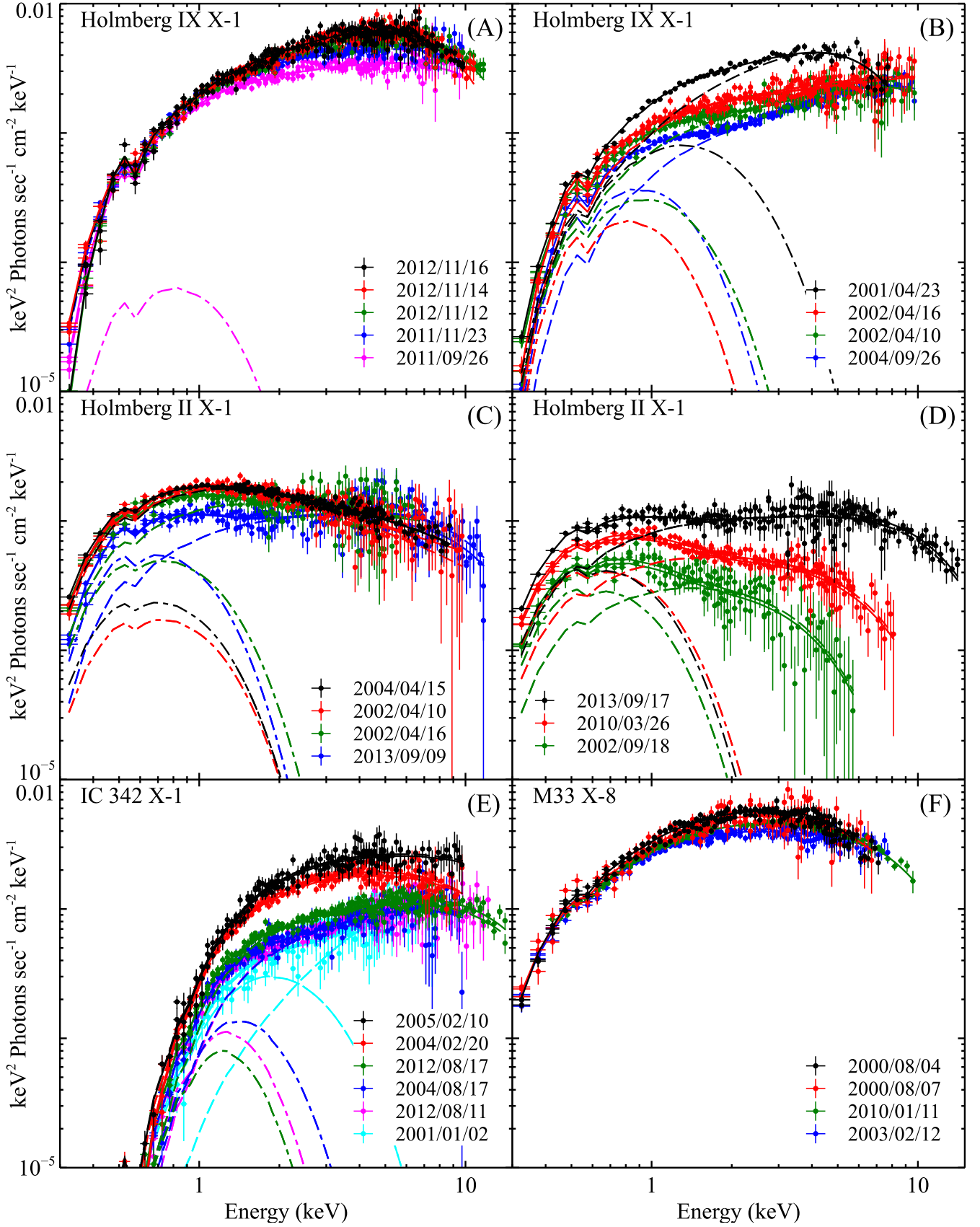


Figure 3. Spectra obtained from other four ULXs, presented in the same way as those of NGC 1313 X-1. For clarity, the spectra of Holmberg IX X-1 and Holmberg II X-1 are divided at the luminosity of $1.5 \times 10^{40} \text{ erg sec}^{-1}$ and $5 \times 10^{39} \text{ erg sec}^{-1}$, respectively.

Table 3. Parameters obtained from the spectral fitting.

Date ^a YY/MM/DD	N_{H}^{b}	T_{e} (keV)	Γ	τ^{c}	T_{in} or $T_{\text{in1}}^{\text{d}}$ (keV)	$R_{\text{raw}}^{\text{e}}$ or $R_{\text{raw1}}^{\text{i}}$	$T_{\text{in2}}^{\text{j}}$ (keV)	$R_{\text{tot}}^{\text{f}}$	$L_{\text{disk}}^{\text{g}}$	L_{X}^{h}	χ^2/ν (ν)
NGC 1313 X-1											
03/12/21	$3.2^{+1.3}_{-0.9}$	$1.8^{+1.6}_{-0.4}$	2.1 ± 0.2	12	$0.18^{+0.08}_{-0.04}$	$7.4^{+18.0}_{-5.2}$	–	$9.4^{+14.4}_{-4.1}$	12.0	10.8	0.82 (72)
03/12/23	$2.7^{+0.7}_{-0.6}$	> 1.9	$1.96^{+0.08}_{-0.06}$	> 11	$0.22^{+0.07}_{-0.05}$	$3.3^{+4.3}_{-1.8}$	–	$4.6^{+3.1}_{-1.3}$	6.4	13.8	0.93 (67)
04/01/08	3 ± 1	> 2.6	$2.31^{+0.09}_{-0.34}$	> 8	$0.18^{+0.08}_{-0.03}$	7.0^{+11}_{-5}	–	$8.7^{+8.8}_{-4.0}$	10.2	7.5	0.94 (207)
04/01/16	$2.8^{+1.0}_{-0.7}$	$2.6^{+2.6}_{-1.1}$	$2.2^{+0.2}_{-0.3}$	9.3	$0.21^{+0.12}_{-0.06}$	$3.1^{+9.0}_{-1.9}$	–	$4.7^{+5.9}_{-1.2}$	5.5	8.4	1.12 (212)
04/06/05	$2.6^{+0.8}_{-0.6}$	$2.0^{+0.7}_{-0.4}$	2.1 ± 0.1	11	$0.19^{+0.12}_{-0.04}$	< 8.6	–	$5.6^{+4.4}_{-1.5}$	5.3	11.4	1.05 (227)
04/08/23	$2.8^{+0.6}_{-0.5}$	$0.9^{+0.2}_{-0.2}$	$2.0^{+0.5}_{-0.8}$	19	$0.22^{+0.05}_{-0.04}$	$4.0^{+3.2}_{-0.5}$	–	$4.4^{+3.0}_{-1.4}$	5.9	3.3	1.16 (167)
04/11/23	$1.7^{+0.5}_{-0.4}$	$2.0^{+8.2}_{-0.6}$	$1.7^{+0.2}_{-0.3}$	16	$0.29^{+0.08}_{-0.06}$	$1.4^{+0.8}_{-0.5}$	–	$1.8^{+0.6}_{-0.4}$	3.0	6.4	1.26 (212)
05/02/07	$3.0^{+1.0}_{-0.8}$	3^{+3}_{-1}	$1.9^{+0.1}_{-0.2}$	11	$0.185^{+0.05}_{-0.03}$	6^{+7}_{-3}	–	$6.3^{+6.3}_{-2.7}$	5	5.8	1.18 (195)
05/10/15	$2.9^{+0.8}_{-0.9}$	1.6 ± 0.1	1.75 ± 0.05	17	$0.17^{+0.05}_{-0.02}$	$7.2^{+8.4}_{-2.5}$	–	10^{+13}_{-9}	10.6	24.7	1.35 (127)
	2.6 ± 0.5	> 2.7	$2.7^{+0.2}_{-0.6}$	> 7	0.22 ± 0.02	$4.5^{+3.4}_{-2.5}$	$0.9^{+0.1}_{-0.2}$	0.30 ± 0.01	8	24.7	1.23 (135)
06/03/06	$3.2^{+0.8}_{-0.7}$	$1.5^{+0.2}_{-0.1}$	1.92 ± 0.09	15	$0.17^{+0.04}_{-0.03}$	$12.0^{+14.0}_{-7.0}$	–	15^{+6}_{-3}	24.3	31.8	1.41 (77)
	$2.7^{+0.4}_{-0.4}$	> 1.0	$3.0^{+0.5}_{-0.9}$	> 11	0.23 ± 0.03	$5.7^{+7.7}_{-4.8}$	$0.8^{+0.1}_{-0.2}$	0.70 ± 0.03	26	31.8	1.26 (71)
06/10/15	$2.4^{+0.2}_{-0.2}$	$2.6^{+0.3}_{-0.3}$	1.70 ± 0.03	14	0.20 ± 0.01	$3.5^{+3.8}_{-1.5}$	–	$4.0^{+0.9}_{-1.2}$	2.7	6.6	1.28 (227)
08/12/05	$1.7^{+0.6}_{-0.5}$	$2.3^{+0.5}_{-0.3}$	$1.7^{+0.05}_{-0.06}$	15	$0.22^{+0.04}_{-0.03}$	$2.7^{+1.8}_{-1.1}$	–	$3.3^{+1.5}_{-0.9}$	3.3	7.1	1.15 (189)
12/12/16	2.0 ± 0.2	$2.6^{+0.2}_{-0.1}$	1.73 ± 0.02	13	$0.24^{+0.02}_{-0.01}$	$2.0^{+0.4}_{-0.3}$	–	$2.5^{+0.3}_{-0.3}$	2.7	6.6	1.30 (266)
12/12/22	2.0 ± 0.1	2.6 ± 0.1	$1.72^{+0.02}_{-0.03}$	13	0.25 ± 0.01	1.9 ± 0.3	–	$2.4^{+0.3}_{-0.2}$	2.9	6.8	1.13 (258)
13/06/08	$2.2^{+0.8}_{-0.6}$	120^{+120}_{-50}	$1.83^{+0.08}_{-0.04}$	> 13	$0.21^{+0.06}_{-0.04}$	$2.8^{+3.8}_{-1.5}$	–	$3.6^{+2.5}_{-1.2}$	3.3	6.6	1.05 (82)
14/05/27 (Low)	4.4 ± 0.9	$1.6^{+0.3}_{-0.2}$	2.19 ± 0.1	13	$0.13^{+0.02}_{-0.01}$	28.1^{+21}_{-14}	–	30^{+23}_{-15}	33.8	10.6	1.35 (187)
	3.3 ± 0.1	> 2.5	$3.1^{+0.2}_{-0.6}$	> 6.2	$0.17^{+0.02}_{-0.01}$	$10.0^{+13.3}_{-7.9}$	$0.62^{+0.06}_{-0.12}$	$0.50^{+0.03}_{-0.02}$	4.8	10.6	1.35 (192)
14/05/27 (Mid)	4.6 ± 1.4	$1.6^{+0.3}_{-0.2}$	2.1 ± 0.1	14	$0.13^{+0.02}_{-0.01}$	$35.0^{+41.1}_{-19}$	–	37^{+38}_{-21}	51.3	15.0	1.04 (189)
	3.0 ± 0.1	> 2.5	$2.7^{+0.6}_{-0.5}$	> 5	$0.17^{+0.05}_{-0.02}$	$10.9^{+22.9}_{-9.8}$	$0.7^{+0.1}_{-0.2}$	$0.49^{+0.05}_{-0.04}$	7.7	15.0	0.99 (189)
14/05/27 (High)	$4.5^{+0.9}_{-1.0}$	$1.8^{+0.2}_{-0.1}$	1.81 ± 0.06	15	0.13 ± 0.01	$39.3^{+25.5}_{-18.2}$	–	42^{+25}_{-18}	63.5	28.4	1.08 (193)
	2.3 ± 0.1	$2.3^{+1.3}_{-0.3}$	$2.0^{+0.3}_{-0.2}$	11	$0.18^{+0.05}_{-0.03}$	$9.0^{+17.8}_{-8.3}$	$0.7^{+0.3}_{-0.2}$	$0.54^{+0.05}_{-0.03}$	11.1	28.3	1.01 (197)
IC 342 X-1											
01/01/02	$1.9^{+0.3}_{-0.7}$	$1.7^{+1.7}_{-0.3}$	< 1.68	> 18	$0.6^{+0.2}_{-0.4}$	$0.3^{+3.6}_{-0.3}$	–	$0.3^{+3.2}_{-0.1}$	1.3	3.1	0.89 (189)
04/02/20	$7.3^{+1.3}_{-1.5}$	$2.8^{+2.2}_{-0.6}$	$2.02^{+0.1}_{-0.09}$	10	0.15 ± 0.02	$17.9^{+17.0}_{-10.4}$	–	19^{+14}_{-9}	23.8	7.1	1.12 (237)
	2.5 (fixed)	$2.4^{+1.1}_{-0.5}$	$1.9^{+0.1}_{-0.2}$	12	0.5 ± 0.1	< 0.3	–	$0.34^{+0.02}_{-0.09}$	0.7	3.1	1.27 (228)
04/08/17	$3.4^{+1.3}_{-0.9}$	$2.5^{+1.5}_{-0.6}$	$1.7^{+0.1}_{-0.2}$	14	$0.32^{+0.1}_{-0.09}$	$0.9^{+1.1}_{-0.5}$	–	$1.1^{+0.9}_{-0.4}$	1.6	3.4	1.15 (229)
05/02/10	$2.3^{+0.8}_{-0.5}$	$3.3^{+3.4}_{-1.5}$	< 2.1	> 9	$0.6^{+0.3}_{-0.1}$	< 0.4	–	$0.38^{+0.03}_{-0.28}$	2.4	9.5	0.93 (197)
12/08/11	4.2 ± 0.8	$3.2^{+1.3}_{-0.6}$	$1.70^{+0.05}_{-0.06}$	12	$0.24^{+0.04}_{-0.03}$	$2.0^{+1.6}_{-0.9}$	–	$2.4^{+1.3}_{-0.8}$	2.5	3.54	0.92 (275)
12/08/17	4.1 ± 1.0	3.0 ± 0.2	1.84 ± 0.05	11	$0.22^{+0.07}_{-0.03}$	$2.2^{+2.6}_{-1.4}$	–	$2.9^{+2.0}_{-1.0}$	2.54	4.0	1.07 (291)
Holmberg IX X-1											
01/04/23	$1.1^{+0.4}_{-0.2}$	1.3 ± 0.2	< 1.7	> 20	0.4 ± 0.2	$0.7^{+0.5}_{-0.2}$	–	$1.0^{+0.4}_{-0.2}$	3.3	17.4	1.18 (72)
02/04/10	$1.1^{+0.3}_{-0.2}$	$2.7^{+1.1}_{-0.5}$	$1.68^{+0.05}_{-0.07}$	14	$0.27^{+0.05}_{-0.04}$	$1.4^{+0.8}_{-0.4}$	–	$2.0^{+0.5}_{-0.3}$	2.7	10.1	1.06 (237)
02/04/16	$1.5^{+0.5}_{-0.4}$	> 3.5	$1.78^{+0.05}_{-0.03}$	< 11	$0.20^{+0.04}_{-0.03}$	$2.6^{+2.5}_{-0.3}$	–	$4.2^{+1.3}_{-0.5}$	3.6	11.8	1.09 (237)
04/09/26	1.6 ± 0.2	2.6 ± 0.2	1.55 ± 0.02	16	0.23 ± 0.02	$2.3^{+0.6}_{-0.5}$	–	$2.9^{+0.8}_{-0.4}$	3.3	9.0	1.16 (213)
11/09/26	$1.5^{+0.4}_{-0.3}$	$2.6^{+0.6}_{-0.3}$	1.84 ± 0.03	12	$0.20^{+0.09}_{-0.05}$	< 4.7	–	$4.3^{+1.1}_{-0.5}$	3.8	16.7	1.05 (237)
11/11/23	$1.1^{+0.2}_{-0.1}$	$2.6^{+0.4}_{-0.3}$	$1.82^{+0.04}_{-0.03}$	13	0.33 ± 0.08	< 0.5	–	$1.7^{+0.1}_{-0.1}$	4.4	20.7	1.09 (237)
12/11/12	0.7 ± 0.1	2.1 ± 0.1	$1.77^{+0.07}_{-0.05}$	14	0.55 ± 0.09	< 0.5	–	$0.67^{+0.01}_{-0.03}$	5.9	22.9	1.18 (287)
12/11/14	$1.1^{+0.4}_{-0.3}$	1.62 ± 0.05	1.57 ± 0.02	20	$0.24^{+0.1}_{-0.08}$	< 2.3	–	$2.9^{+0.7}_{-0.3}$	3.6	24.5	1.22 (276)
12/11/16	0.4 ± 0.2	$2.0^{+0.3}_{-0.1}$	$1.87^{+0.3}_{-0.1}$	18	0.77 ± 0.2	< 0.4	–	0.38 ± 0.01	7.2	24.0	1.23 (270)
Holmberg II X-1											
02/04/10	0.5 ± 0.2	> 3.8	$2.59^{+0.05}_{-0.14}$	< 18	0.21 ± 0.05	< 2.4	–	$3.9^{+0.3}_{-0.6}$	3.8	8.9	1.13 (227)
02/04/16	0.4 ± 0.2	> 2.0	$2.2^{+0.3}_{-0.2}$	< 11	$0.22^{+0.03}_{-0.02}$	$2.3^{+1.2}_{-0.6}$	–	$3.5^{+0.8}_{-0.4}$	3.8	8.7	1.20 (202)
02/09/18	$0.4^{+0.4}_{-0.3}$	$0.8^{+1.0}_{-0.3}$	< 2.6	> 15	$0.19^{+0.06}_{-0.04}$	$2.6^{+2.0}_{-0.9}$	–	$3.0^{+1.7}_{-0.8}$	3.7	1.9	0.98 (147)
04/04/15	0.4 ± 0.1	$3.7^{+3.5}_{-1.0}$	$2.39^{+0.08}_{-0.07}$	7	0.21 ± 0.03	$1.9^{+0.5}_{-0.3}$	–	4.1 ± 0.2	4.2	9.3	1.2 (160)
10/03/26	0.3 ± 0.1	$1.4^{+0.3}_{-0.2}$	2.1 ± 0.1	15	0.21 ± 0.02	$2.4^{+0.5}_{-0.4}$	–	$2.9^{+0.4}_{-0.3}$	2.1	3.5	1.09 (209)
13/09/09	0.7 ± 0.3	$2.2^{+0.5}_{-0.3}$	1.88 ± 0.07	13	$0.19^{+0.03}_{-0.02}$	$3.8^{+1.9}_{-1.2}$	–	$4.7^{+1.6}_{-1.0}$	3.7	7.0	1.05 (246)
13/09/17	$0.3^{+0.3}_{-0.2}$	$2.4^{+0.2}_{-0.1}$	1.92 ± 0.06	12	0.20 ± 0.03	$2.8^{+1.7}_{-1.0}$	–	$3.8^{+1.2}_{-0.7}$	2.9	6.9	1.03 (258)

Notes: ^aDate of the observations. ^bIntrinsic column density of equivalent Hydrogen in units of 10^{21} cm⁻². ^cOptical depth of the coronal electron cloud. See text for the statistical uncertainty. ^dInner-disk temperature or that at the radius where the corona is truncated (see text). ^e Apparent inner-disk radius of the un-scattered accretion disk component in units of 1000 km. ^f Inner-disk radius of the overall disk component in units of 1000 km. Calculated from equation 1. ^g Bolometric luminosity of the accretion disk component in units of 10^{39} erg sec⁻¹. ^h Absorbed 0.3 – 10 keV band luminosity in units of 10^{39} erg sec⁻¹. ⁱ Apparent inner-disk radius of the outer-disk region in units of 1000 km. ^j Inner-disk temperature of the model representing the inner part of the disk in the alternative model (see text).

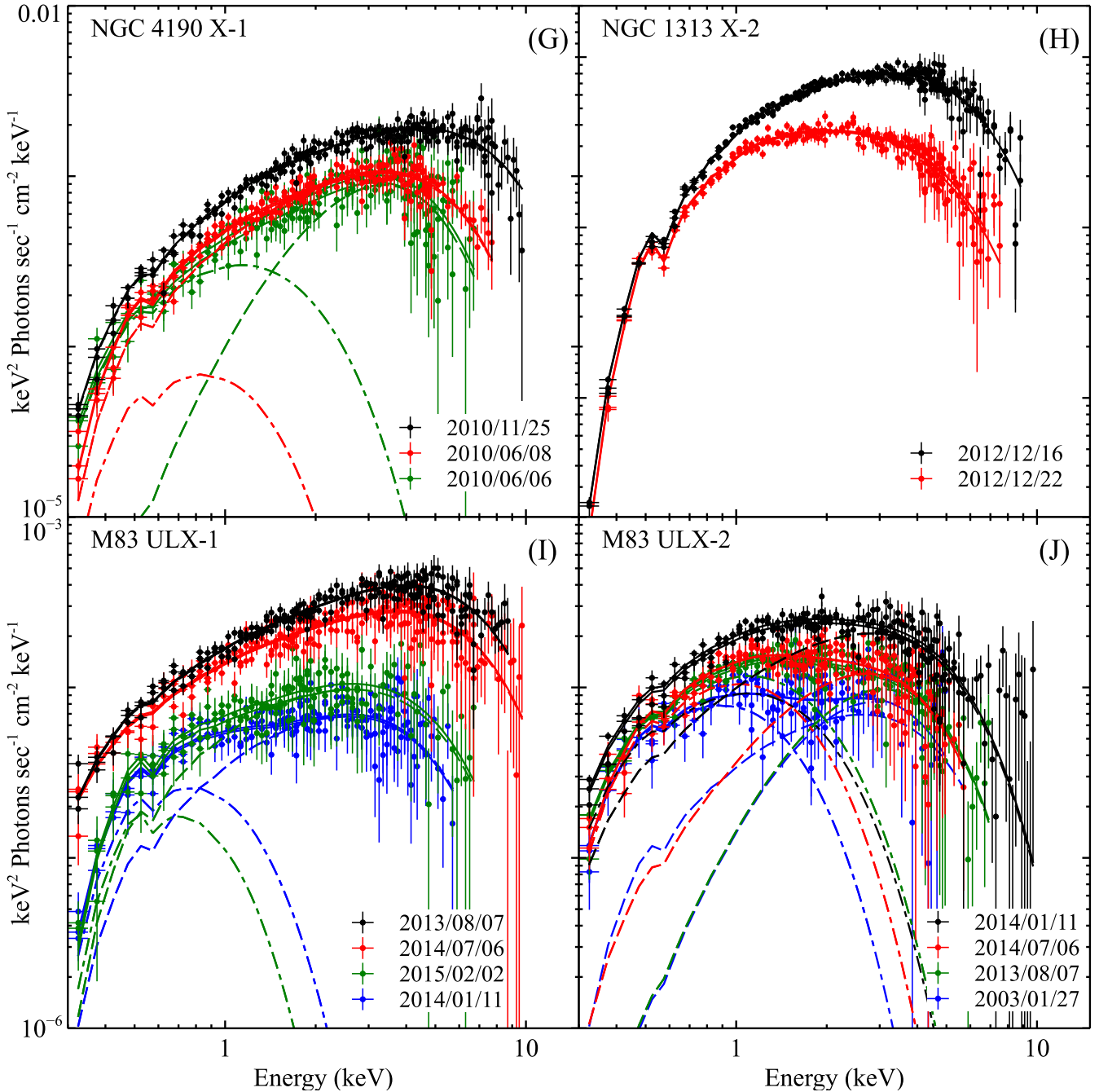


Figure 3 – *continued* Spectra obtained from the remaining four sources.

4 DISCUSSION

4.1 Summary of the Results

Utilizing *Suzaku*, *XMM-Newton*, and *NuSTAR*, we studied 56 spectra of 9 representative ULXs, and obtained the following results.

- (i) Of the 56 spectra, 3 can be classified into the SPL state, 24 into the HPL state, and the remaining 19 into the MCD state. When a source resided in multiple states, its luminosity was always in the order of SPL < HPL < MCD.
- (ii) In any spectral state, the spectra in the present sample were all successfully reproduced by a single continuum

model (the MCD+THC model), requiring no additional local feature components.

- (iii) Regardless of the spectral states, the 9 sources are all inferred to harbor cool ($T_e \sim 1.5 - 3$ keV) and optically-thick ($\tau > 10$) corona, in agreement with the results of some previous works (e.g., Miyawaki et al. 2009).
- (iv) The spectral transition from the SPL to HPL states is characterized by an increase in the T_e/T_{in} ratio, whereas that from the HPL to MCD states by an increase in T_{in} and a marked decrease in the directly-visible-disk fraction.
- (v) All sources showed stable and low absorption as $N_H \sim$

Table 3 – *continued*

Date ^a YY/MM/DD	N_{H}^{b}	T_{e} (keV)	Γ	τ^{c}	T_{in} or $T_{\text{in1}}^{\text{d}}$ (keV)	$R_{\text{raw}}^{\text{e}}$ or $R_{\text{raw1}}^{\text{i}}$	$T_{\text{in2}}^{\text{j}}$ (keV)	$R_{\text{tot}}^{\text{f}}$	$L_{\text{disk}}^{\text{g}}$	L_{X}^{h}	χ^2/ν (ν)
M33 X-8											
00/08/04	$0.3^{+0.2}_{-0.1}$	$1.19^{+0.2}_{-0.08}$	$1.8^{+0.2}_{-0.1}$	19	0.4 ± 0.1	< 0.2	–	$0.40^{+0.02}_{-0.22}$	0.5	1.7	1.21 (204)
00/08/07	$0.2^{+0.2}_{-0.1}$	$1.6^{+1.6}_{-0.7}$	< 3.2	> 8	$0.53^{+0.3}_{-0.07}$	< 0.3	–	$0.22^{+0.01}_{-0.15}$	0.4	1.6	1.12 (172)
03/02/12	$0.25^{+0.09}_{-0.08}$	$2.2^{+1.1}_{-0.4}$	2.1 ± 0.1	11	$0.41^{+0.08}_{-0.04}$	< 0.1	–	$0.34^{+0.01}_{-0.04}$	0.3	1.4	1.10 (213)
10/01/11	0.12 ± 0.08	$1.9^{+0.2}_{-0.1}$	$2.06^{+0.08}_{-0.06}$	12	0.5 ± 0.05	< 0.06	–	$0.230^{+0.003}_{-0.011}$	0.3	1.5	1.27 (136)
M83 ULX-1											
13/08/07	< 0.4	$1.35^{+0.1}_{-0.09}$	$1.58^{+0.05}_{-0.1}$	22	$0.28^{+0.16}_{-0.03}$	< 0.6	–	$0.75^{+0.03}_{-0.08}$	0.5	3.1	1.08 (222)
14/01/11	$0.8^{+0.7}_{-0.5}$	$0.9^{+0.3}_{-0.2}$	1.6 ± 0.3	28	$0.21^{+0.09}_{-0.05}$	$0.8^{+1.2}_{-0.4}$	–	$1.0^{+1.0}_{-0.4}$	0.3	1.1	0.82 (171)
14/07/06	< 8.2	1.3 ± 0.1	$1.6^{+0.07}_{-0.1}$	21	$0.28^{+0.2}_{-0.05}$	< 0.3	–	$0.67^{+0.02}_{-0.15}$	0.4	2.3	1.03 (227)
15/02/02	$1.1^{+1.1}_{-0.8}$	$0.9^{+0.3}_{-0.3}$	$1.7^{+0.2}_{-0.4}$	23	$0.17^{+0.05}_{-0.05}$	< 0.6	–	$2.0^{+3.4}_{-1.2}$	0.5	0.8	0.81 (150)
M83 ULX-2											
03/01/27	$0.4^{+0.4}_{-0.3}$	$0.71^{+0.2}_{-0.07}$	< 1.7	> 27	0.29 ± 0.06	$0.7^{+0.3}_{-0.2}$	–	$0.7^{+0.3}_{-0.2}$	0.4	0.8	1.26 (143)
13/08/07	$0.2^{+0.2}_{-0.1}$	$0.76^{+0.2}_{-0.05}$	< 2.1	> 19	$0.40^{+0.05}_{-0.1}$	0.4 ± 0.1	–	$0.4^{+1.1}_{-0.1}$	0.5	1.2	1.09 (195)
14/01/11	$0.1^{+0.2}_{-0.1}$	$0.9^{+0.2}_{-0.1}$	< 2.1	> 17	0.4 ± 0.1	< 0.5	–	$0.5^{+0.1}_{-0.3}$	0.8	2.5	1.12 (217)
14/07/06	0.5 ± 0.3	$0.73^{+0.3}_{-0.08}$	< 2.1	20.1	0.3 ± 0.1	$0.5^{+0.3}_{-0.2}$	–	$0.6^{+0.3}_{-0.2}$	0.4	1.2	1.15 (177)
NGC 4190 X-1											
10/06/06	0.5 ± 0.4	$0.83^{+0.15}_{-0.04}$	< 2.2	> 18	$0.41^{+0.08}_{-0.2}$	$0.5^{+0.6}_{-0.1}$	–	$0.5^{+0.6}_{-0.1}$	0.9	3.6	1.15 (202)
10/06/08	$0.9^{+0.6}_{-0.4}$	$1.08^{+0.09}_{-0.1}$	$1.55^{+0.09}_{-0.12}$	25	$0.2^{+0.2}_{-0.1}$	< 1.7	–	$1.4^{+0.9}_{-0.4}$	0.4	4.5	1.19 (197)
10/11/25	0.6 ± 0.2	$1.6^{+0.2}_{-0.3}$	< 1.7	> 18	$0.42^{+0.5}_{-0.1}$	< 0.5	–	$0.63^{+0.03}_{-0.50}$	1.2	8.5	1.08 (237)
NGC 1313 X-2											
12/12/16	$1.7^{+0.3}_{-0.2}$	1.17 ± 0.05	$1.69^{+0.05}_{-0.08}$	21	$0.28^{+0.09}_{-0.06}$	$0.6^{+0.5}_{-0.2}$	–	$1.3^{+0.2}_{-0.1}$	1.3	4.8	1.16 (239)
12/12/22	$1.9^{+0.5}_{-0.3}$	1.07 ± 0.09	$2.02^{+0.08}_{-0.13}$	17	$0.21^{+0.08}_{-0.06}$	< 2.4	–	$2.0^{+0.7}_{-0.5}$	1.0	2.2	1.14 (229)

Notes: ^aDate of the observations. ^bIntrinsic column density of equivalent Hydrogen in units of 10^{21} cm^{-2} . ^cOptical depth of the coronal electron cloud. See text for the statistical uncertainty. ^dInner-disk temperature or that at the radius where the corona is truncated (see text). ^eApparent inner-disk radius of the un-scattered accretion disk component in units of 1000 km. ^fInner-disk radius of the overall disk component in units of 1000 km. Calculated from equation 1. ^gBolometric luminosity of the accretion disk component in units of $10^{39} \text{ erg sec}^{-1}$. ^hAbsorbed 0.3–10 keV band luminosity in units of $10^{39} \text{ erg sec}^{-1}$. ⁱApparent inner-disk radius of the outer-disk region in units of 1000 km. ^jInner-disk temperature of the model representing the inner part of the disk in the alternative model (see text).

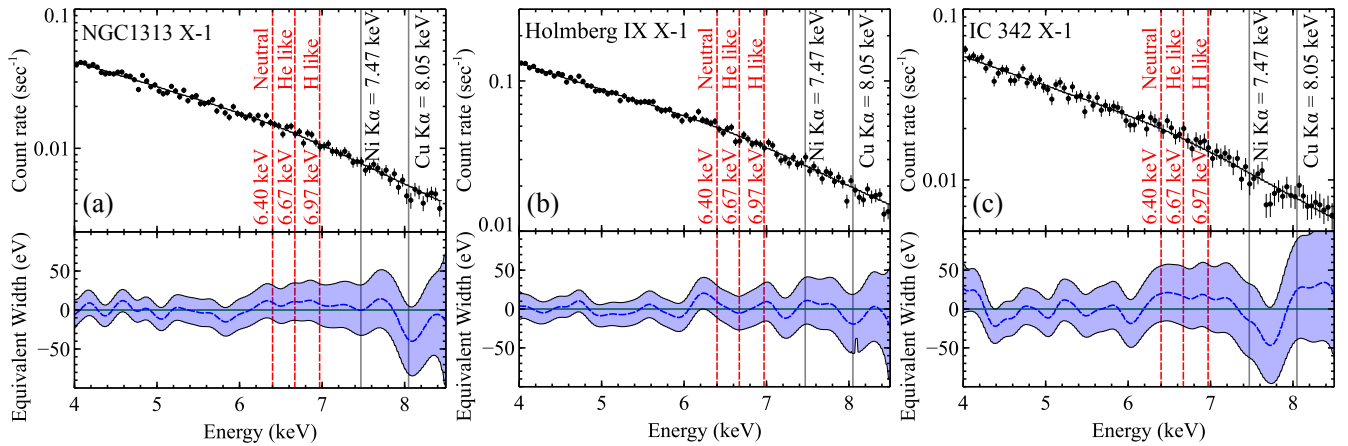


Figure 4. Stacked PN spectra of NGC 1313 X-1 (panel a), Holmberg IX X-1 (panel b), and IC 342 X-1 (panel c), fitted with a cutoff power law model (top panels). The bottom panels indicate the allowed range of the line equivalent width, where the blue dashed line and the light blue band represent the best fit value and the 99% confidence range, respectively. Positive and negative equivalent widths specify emission and absorption lines, respectively.

10^{21} cm^{-2} , where the Galactic line-of-sight contribution is separately modeled and removed.

- (vi) In three sources with high signal statistics, Holmberg IX X-1, IC 342 X-1, and NGC 1313 X-1, stringent upper limits of 30 – 55 eV in EW were obtained for narrow Fe K-shell emission/absorption lines.

4.2 Spectral State Transitions and State Indicators

In section 3, many of the sources in our sample showed multiple spectral states from SPL, HPL, and MCD, with the luminosity increasing in this order [section 4.1 item (i)]. At the same time, the 56 spectra were all fitted successfully with a single unified model, namely, the MCD +THC model [section 4.1 item (ii)]. Then, as already suggested by section 4.1 item (iv), we must be able to utilize the best-fit model parameters to quantitatively specify the spectral states, instead of just looking by eyes at their spectral shapes.

To characterize the spectral shapes of ULXs, we introduce three quantities, each derived from the obtained model parameters. They are the temperature ratio $Q \equiv T_e/T_{\text{in}}$, the coronal covering fraction

$$F \equiv 1 - (R_{\text{raw}}/R_{\text{tot}})^2, \quad (3)$$

and the Compton y -parameter. Here, Q represents the balance point between heating and cooling of the coronal electrons (Zhang et al. 2016), and F describes the fractional area of the accretion disk covered by the corona (Kobayashi et al. 2016). Although the radii R_{raw} and R_{thc} are affected by distance uncertainties and the unknown inclination angle of the accretion disk, these should cancel out by taking ratios in the calculation of F . Hence, F is a parameter which is directly comparable among different sources.

The third parameter, y , needs some caution. If the coronal electron temperature T_e is much higher than that of the seed photons (i.e., $T_e \gg T_{\text{in}}$ in the present case), the y -parameter is generally approximated, with the help of equation 2, as $y \sim 4kT_e\tau(1 + \tau/3)/m_e c^2 = 4/[(0.5 + \Gamma)^2 - 2.5]$ in an optically thick condition, where k and m_e are the Boltzmann constant and the electron mass, respectively. However, the temperature of $T_e \sim 2 \text{ keV}$ found in our sample is rather too low to be regarded as $T_e \gg T_{\text{in}}$, because it is at most only 10 times higher than the seed photon temperature, $T_{\text{in}} \sim 0.2 \text{ keV}$. To take this closeness into account, we hereafter modify the definition as

$$y \equiv \frac{4k(T_e - T_{\text{in}})}{m_e c^2} \tau(1 + \tau/3) = \frac{4k}{[(0.5 + \Gamma)^2 - 2.5]} \left(\frac{T_e - T_{\text{in}}}{T_e} \right), \quad (4)$$

following Zhang et al. (2016) who studied similarly cool and thick coronae.

In terms of these physical/geometrical parameters, let us try classifying the three spectral states in an objective way. Since there are three states, we may need at least two parameters, of which one would be Q itself because of section 4.1 item (iv). As the other, the product $y \times F$ is expected to be promising: F describes how much fraction of the disk photons get Comptonized, whereas y (equation 4) specifies the relative energy gain of each Comptonized photon, so their product would provide a good measure of the degree of Comptonization of all photons emerging from each system.

In figure 5, we present a scatter plot between $y \times F$

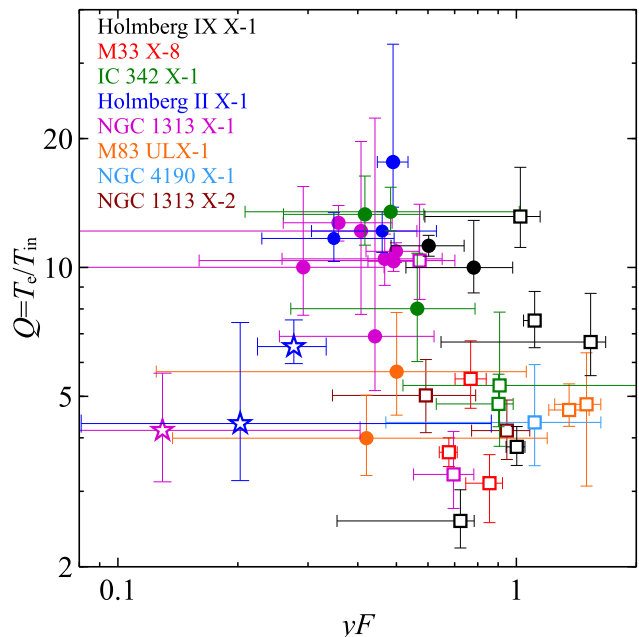


Figure 5. A scatter plot between yF and Q for the present spectra. The open stars, the filled circles, and the open squares represent the data in the SPL, the HPL, and the MCD states, respectively. Colors specify the different objects. The error bars correspond to 68% confidence level.

and Q for 39 spectra. For clarity, we omitted 17 data points with poor statistics, in which either T_e or Γ were unconstrained. The spectral states, already identified by their overall spectral appearance, are distinguished by different symbols. Thus, the plot successfully accommodates the SPL and MCD data points at $Q \leq 10$ due to the closeness between T_{in} and T_e , and those in the HPL state at $Q > 10$ due to the large difference between the two temperatures. At the same time, we observe that the SPL, HPL, and MCD data points generally appear on figure 5 as the increasing order of the yF product. This means that the overall Comptonization effect is highest in the MCD state, and lowest in the SPL state. As a result of these two tendencies, the data points draw a convex locus on the (yF, Q) plane. Thus, the yF vs. Q plot has successfully distinguished the three characteristic spectral states in a quantitative way, even though the errors are rather large.

4.3 Discrimination of NS ULX Candidates

During the revision of this paper, weak coherent pulsations with a period of $\sim 1.5 \text{ s}$ were discovered in some of the latest X-ray observations of NGC 1313 X-2 (Sathyaprakash et al. 2019). Although the statistical significance of the detection is still marginal ($3 - 4\sigma$), the result strongly suggests that the source, long believed to be an accreting BH, actually harbors an NS as the mass accretor. As we have seen so far, the spectra of NGC 1313 X-2 are apparently similar to those of the other ULXs in the MCD state. Hence, there arises a possibility that our sample could still be contaminated by NS ULXs, besides NGC 1313 X-2. To minimize this risk, we need

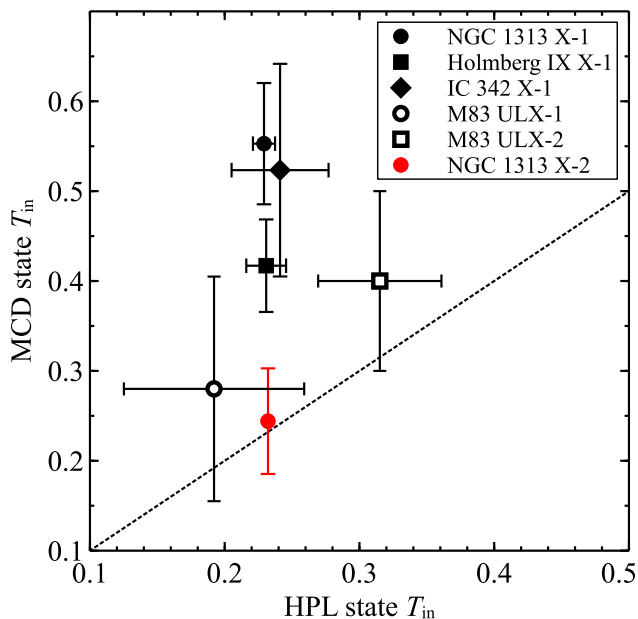


Figure 6. Our sample objects, plotted on the plane of the error weighted mean T_{in} in the HPL state (abscissa) and that in the MCD state (ordinate). The dashed line indicates that the two temperatures are equal. The plot excludes those sources which did not make transitions between the HPL and the MCD states in our observations. See text for the treatment of NGC 1313 X-2 (shown in red).

to look for some additional ways to distinguish potential NSs from the rest.

As an attempt, in figure 6 we plot our sample objects on the plane of the error-weighted mean T_{in} in the HPL states and that in the MCD state. Since the present sample does not include any spectra of NGC 1313 X-2 in the HPL state, we took its HPL T_{in} values from [Pintore & Zampieri \(2012\)](#), in which several HPL state spectra of NGC 1313 X-2 were analyzed with the same type of spectral modeling as the present work. Thus, most of the sources show a significantly higher T_{in} in the MCD state than in the HPL state, whereas NGC 1313 X-2 exhibits insignificant change in T_{in} between the two states. Although the physical origin of this difference is unknown, the result may allow us to discriminate NGC 1313 X-2 (possibly M83 ULX-1 as well) from the other objects in the sample. Since no other NS ULXs are reported to have made transitions between the HPL and MCD states, we are not sure at present whether this discrimination is general or not, but we employ figure 6 as a criterion to remove NGC 1313 X-2 from our subsequent discussion.

4.4 State Transition Luminosities

As described in section 1, one of our interests is how the spectral states are distributed against the source luminosity. Since we have shown above that the two new parameters Q and yF are good indicators of their spectral states, we present in figure 7 their behavior as a function of the 0.3–20 keV luminosity L_X .

In contrast to the relatively well-organized locus seen in figure 5, the L_X vs. Q and L_X vs. yF plots, figure 7 (A)

and figure 7 (B) respectively, both suffer significant scatter of the data points. In fact, almost no correlation is seen in figure 7 (A), and the distribution ranges of the three states, represented by three colored horizontal bars in figure 7 (B), heavily overlaps with one another. We consider that this is because the individual sources reside in a particular spectral state (i.e., similar values in Q or yF) at rather different luminosities. In fact, M33 X-8 exhibit a series of MCD-state spectra (open squares) at $L_X \sim 1.5 \times 10^{39}$ erg sec $^{-1}$, whereas the sources such as Holmberg IX X-1 and NGC 1313 X-1 at $L_X \sim 3 \times 10^{40}$ erg sec $^{-1}$. Then, the data scatter in these panels would diminish if we scale L_X by appropriate factors that are specific to the individual sources.

As presented in panels (C) and (D) of figure 7, we hence scaled L_X of 7 sources (except NGC 1313 X-1), by a factor which brings the behavior of each source to line up with that of NGC 1313 X-1. We scanned the scaling factors of the individual sources over appropriate ranges, and searched for the optimum values that minimize the overall data scatter in L_X in the following way. First, in the i -th spectral state ($i = 1, 2, 3$), the average L_X of NGC 1313 X-1 was chosen as the fiducial value. Then, relative to that value, the standard deviation σ_i of the scaled luminosity of the other spectra in the same state was calculated. Finally, the overall scatter was calculated as $\sigma = \sum_{i=1}^3 \sigma_i$. We have employed the standard deviation rather than chi-square, because errors associated with individual L_X determinations are difficult to estimate and are considered to be relatively similar among the sample spectra. The obtained optimum scaling factors are given in the legends of these panels. As a result, the data scatter in the L_X vs. Q and L_X vs. yF plots have both decreased significantly. At the same time, a good correlation has appeared in figure 7 (C) between yF and the scaled L_X . In figure 7 (D), the three states have become re-distinguishable in terms of Q and yF just as in figure 5. These results indicate that the luminosity renormalization is physically meaningful, and the state-emerging luminosity systematically differs by at least a factor of ~ 16 among the 8 sources.

The canonical BH/NS binary systems also show several spectral states as a function of their luminosity, and the behavior is almost uniquely determined by the Eddington ratio η . For example, the standard High/Soft State are observed typically at $\eta = 0.1 - 0.3$, and so-called Very High State of BHs emerges at $\eta \sim 0.3$ (e.g., [Kubota & Makishima 2004](#); [Tamura et al. 2012](#)). If we assume that this general property widely seen in accreting systems is also shared by ULXs, the luminosity re-normalizing factor which we have employed can be regarded, most naturally, as the $(L_{\text{edd}})_o/L_{\text{edd}}$ ratio of the each source, where $(L_{\text{edd}})_o$ refers to the value of NGC 1313 X-1. In other words, the scaled luminosity can be identified with η , except a common proportionality factor. This implies that L_{edd} of our sample sources also scatters by the same factor (~ 16).

Since L_{edd} is proportional to the mass of the compact object, the difference in L_{edd} directly suggests that the mass of our sample also scatters over a similar range. For example, we may assume that the lowest mass (M33 X-8) of the present ULXs to be $\sim 10 M_\odot$, which is typical of a stellar mass BH. Then, the highest mass in our sample (Holmberg IX X-1) should reach $\sim 160 M_\odot$, which is in the intermediate mass regime. If so, the 8 ULXs (excluding NS ULX

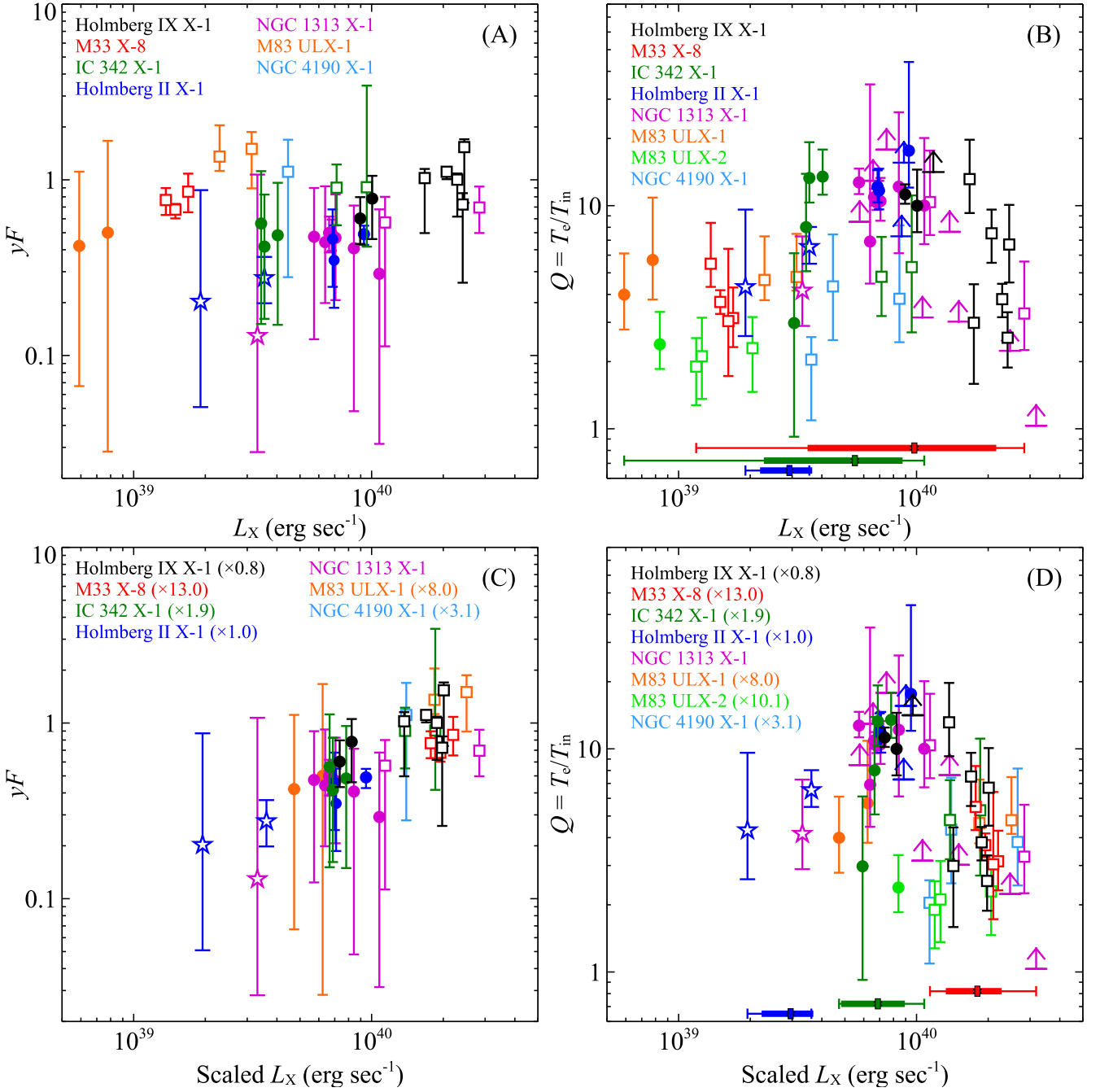


Figure 7. The parameters Q (panel A) and yF (panel B) of the present spectra, shown against the 0.3 – 20.0 keV luminosity L_X . The plotting symbols and the colors are the same as in figure 5. (C) and (D) are the same panels as (A) and (B), respectively, but the luminosity of each source is scaled by a certain factor to match that of NGC 1313 X-1. The scaling factors are shown in the legends. The horizontal bars at the bottom of panels (B) and (D) represent the luminosity distributions of the individual spectral states (blue for SPL, green for HPL, red for MCD). The central markers, thin horizontal lines, and thick bars show their mean values, full distribution ranges, and the standard deviations, respectively.

NGC 1313 X-2 which is very likely to be an NS-ULX) are implied to have a broad mass distribution from $\sim 10 M_\odot$ to $\sim 160 M_\odot$, in qualitative agreement with the latest results from the Gravitational Wave experiments. Thus, unlike the ordinary BH/NS binaries, but somewhat similar to Active Galactic Nuclei, these typical ULXs are suggested to have a wide mass range, of which the highest end will exceed the

generally accepted masses of stellar BHs. The values of R_{in} (table 3), typically of the order of $\sim 10^3$ km, are consistent with this interpretation, even though these estimates are subject to the large statistical (and possibly systematic as well) uncertainties. This argument assumes only a general property which is widely seen in the accreting objects, and do not rely on any particular accretion models. In par-

ticular, the argument does not rely on absolute values of η , and hence should not depend on whether ULXs are super-Eddington or sub-Eddington sources.

4.5 Paucity of local materials

4.5.1 Absorption line features

As revealed in section 3, the present stacked ULX spectra are devoid of spectral evidence for significant materials around the sources. To consider implications of these results, we first compare the strength of the Fe $K\alpha$ absorption lines of the present sample with those obtained in other accreting objects.

Blue-shifted Fe $K\alpha$ absorption lines with high ionization are occasionally seen in spectra of some BH binaries in the High/Soft state (e.g., Miller et al. 2006) and active galactic nuclei (Tombesi et al. 2010). This particular feature is evidently telling us that some “winds” are often launched into our line of sight, presumably from the accretion disks. Since ULXs are as powerful accretors as these objects, it is natural to expect these winds to be also present in ULXs. Hence, many attempts were made to search their spectra for these absorption or emission line features. In particular, stacking analysis similar to ours have been made with other data of bright ULXs (e.g., Walton et al. 2013). Despite these efforts including ours, none of the ULX analyzed showed noticeable signs of the Fe $K\alpha$ absorption lines, except for one particular observation of NGC 1313 X-1 (velocity of $\sim 0.2c$ and EW -61 ± 24 eV; Walton et al. 2016). Furthermore, upper limits on the EW of absorption lines, obtained from the other observations of ULXs, are typically several tens eV like in the present case, which is comparable to or more stringent than the actual detections from BHs in the High/Soft state (20–70 eV; e.g., Ponti et al. 2012; Yamada et al. 2013). Gathering these results together, the disk winds in ULXs are likely to be generally rather weak or transient.

The detection of the blue-shifted highly-ionized lines from NGC 1313 X-1 could be taken as a good evidence for ULXs being supercritical accretion states. In fact, some numerical simulations show that massive disk winds are launched in such an accretion regime (e.g., Kawashima et al. 2012). However, such disk winds are also confirmed in BH binaries that clearly reside in sub-critical regimes (e.g., Miller et al. 2012; Ponti et al. 2012). Furthermore, some sources that are likely to be accreting at supercritical rate are known to yield significant Fe K absorption-edge features as well (e.g., Hagino et al. 2016; Shidatsu et al. 2016), which are not observed from ULXs. Thus, detections of blue-shifted absorption lines would not be regarded as unique evidence of supercritical accretion flows.

4.5.2 Emission line features and low energy absorption

Next, we examine the absorbing column densities N_{H} and the Fe-K line EWs, measured in the present study, utilizing the EW vs N_{H} diagram in figure 8. While the line EW represents the total amount of matter surrounding the source, N_{H} gives the amount of matter in the line of sight. If the matter surrounds the central source spherically and uniformly, these two quantities should be proportional to each other, as shown by the dotted line in figure 8 (Inoue 1985). Since the

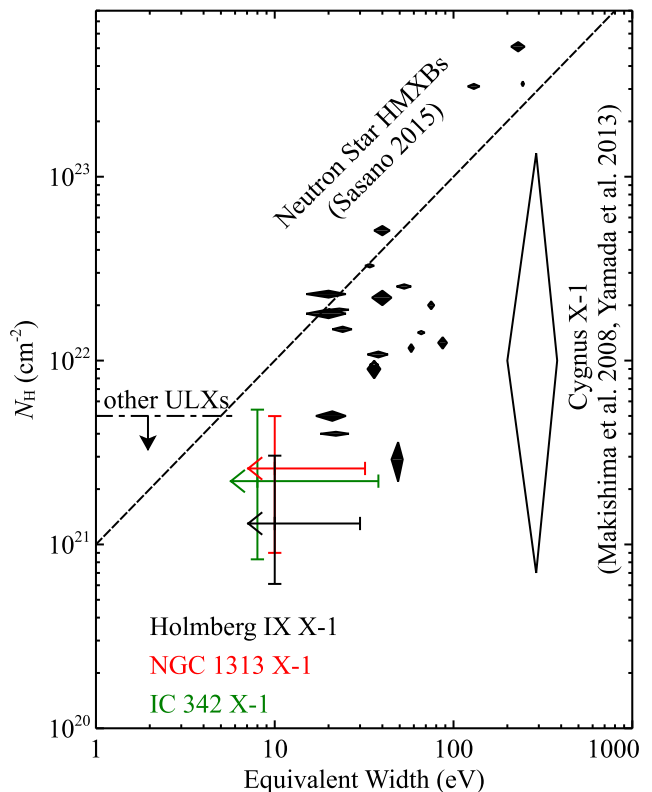


Figure 8. A scatter plot between the Fe $K\alpha$ line equivalent width and the line-of-sight absorption column density N_{H} . The Galactic contributions in N_{H} of ULXs were removed, while those of the other classes of objects are not. The dot-dashed line indicates the maximum value obtained from the present ULX sample. The dashed line represents predictions for isotropic and spherical gas clouds with a solar abundance (Inoue 1985), neglecting self-absorption of the Fe-K lines which become significant at $N_{\text{H}} \gtrsim 10^{23} \text{ cm}^{-2}$

matter distribution is often highly anisotropic, considering both the line EW and N_{H} provides a good tool of diagnostics.

On the plane of EW vs N_{H} , figure 8 compares the present ULX sample with representative Galactic NS/BH binaries (Makishima et al. 2008; Yamada et al. 2013; Sasano 2015). The comparison is limited to High Mass X-ray Binaries (HMBs), i.e., binaries with massive mass-donating stars, because ULXs are generally considered to be similar systems (e.g., Rappaport et al. 2005). Thus, the Galactic HMXBs exhibit strong emission lines with EW of 20–300 eV, and high absorption as $N_{\text{H}} = 1 \times 10^{21} - 7 \times 10^{23} \text{ cm}^{-2}$ which is often highly variable (e.g., two orders of magnitude in Cygnus X-1). These properties of HMXBs are understood by considering that they are immersed, e.g., in thick stellar winds from the donor stars, and only a small fraction of such circum-source matter is captured by the compact component to drive X-ray emission. In contrast, the Fe K lines in the ULXs are weaker than 30–40 eV in EW, and their N_{H} values (after subtracting the Galactic contribution) are all below $8 \times 10^{21} \text{ cm}^{-2}$, and variations by 30% at most. Thus, in addition to the difference in the absorption lines, figure 8 provides another distinction between ULXs and Galactic HMXBs. The result suggests that ULXs do not have such

massive circum-source materials as seen in the other class of HMXBs, including stellar winds from the donor stars, of which only a small fraction is captured by the compact component to drive X-ray emission.

A possible explanation to the apparent difference between the ordinary HMXBs and ULXs would be that the matters around ULXs are highly ionized due to their intense X-ray illumination. Let us examine this possibility. Generally, the ionization degree of a gas under illumination with a luminosity L is represented by the ionization parameter as

$$\xi = \frac{L}{nr^2}, \quad (5)$$

where n and r are the gas density and distance from the X-ray source, respectively. Assuming a gas flow with a nearly-free-fall velocity $v \propto (M/r)^{0.5}$, where M is the object mass, the mass accretion rate can be expressed as

$$\dot{m} \propto \pi r^2 v n \propto \pi r^{1.5} M^{0.5} n. \quad (6)$$

Since the luminosity is given as $L = \zeta \dot{m} c^2$, where ζ is the radiation efficiency, equation (5) can be rewritten, using equation (6), as

$$\xi \propto \frac{\zeta n M^{0.5} r^{1.5}}{nr^2} \propto \zeta \left(\frac{M}{r}\right)^{0.5}. \quad (7)$$

In a wind accretion system, the central object accretes gas within a radius called Bondi radius, where the gravitational pull becomes equivalent to the kinetic energy of the incoming stellar wind. This can be written as $R_B = 2GM/V_w^2$, where G and V_w is the gravitational constant and the velocity of the wind, respectively. By substituting $r = R_B$ in equation (7), we obtain the ionization parameter at the distance of Bondi radius as

$$\xi \propto \zeta V_w, \quad (8)$$

which is sensitive to neither the luminosity nor the mass of the accreting object. Therefore, as long as assuming a wind-fed geometry, we find no reasons to believe that the matters around ULXs are more ionized than those around the ordinary HMXBs. The explanation invoking the matter ionization becomes even more difficult if ULXs are under super-critical accretion, because ζ should be much smaller in such systems (e.g., [Mineshige & Ohsuga 2007](#)). In short, the matter ionization scenario is not favored.

Another common accretion scheme among binary systems is Roche-Lobe overflow (RLO) accretion, in which the companion star is filling its Roche lobe and matters are accreting through the inner Lagrange point. Because the RLO realizes high values of \dot{m} , it is favored to explain the high luminosities of ULXs. In addition, the absorption and reprocessed spectral features are generally expected to be weaker, since less matters are distributed around the binary system than in wind-fed objects.

LMC X-3 is one of the few good examples of RLO-powered BH binaries in HMXB systems ([Soria et al. 2001](#); [Orosz et al. 2014](#)). It consists of a $7 M_\odot$ BH, and a donor star with a mass of $\sim 8 M_\odot$ ([Özel et al. 2010](#)). According to the previous observations, the spectrum of LMC X-3 exhibited low N_H as $< 10^{20} \text{ cm}^{-2}$ ([Soria et al. 2001](#)), which is comparable to what we have seen in the ULXs. On the other hand, the spectrum showed an Fe $K\alpha$ line with an EW ranging between 50 – 80 eV in its Low/Hard state (e.g., [Nowak](#)

[et al. 2001](#), [Wilms et al. 2001](#)); this is clearly stronger than those in the ULXs. Although the example is quite limited, the RLO system in sub-Eddington regimes appears to be somewhat different from ULXs.

How about RLO systems in high-Eddington regimes? SMC X-1 is a luminous RLO powered NS HMXB ([Savonije 1979](#)). Since its luminosity ($3\text{--}5 \times 10^{38} \text{ erg sec}^{-2}$; e.g., [Neilsen et al. 2004](#)) is close to or even higher than its L_{edd} , the source is a good example of a high- η RLO system. The spectrum of SMC X-1 is relatively featureless, bears weak Fe $K\alpha$ lines with an EW of 20–30 eV, and is on average weakly absorbed with N_H of $2 \times 10^{21} \text{ cm}^{-2}$ (e.g., [Naik & Paul 2004](#), [Vrtilek et al. 2005](#)). However, N_H of SMC X-1 is known to vary from $2 \times 10^{22} \text{ cm}^{-2}$ to 10^{23} cm^{-2} through its super-orbital cycle ([Hu et al. 2013](#)), in disagreement with the behavior of ULXs. A similar high- η NS HMXB is Centaurus X-3, which is also likely to be powered via RLO because of its high luminosity. Analyzing *Suzaku* data of this pulsar over its full orbital period of 2.1 days, [Naik et al. \(2011\)](#) detected Fe-K line at 6.4 keV (plus higher-ionization lines) throughout the orbital period, and its EW was always $> 60 \text{ eV}$. Furthermore, even away from the eclipses, the spectra sometimes showed a deep Fe-K absorption edge, which corresponds to N_H of several times 10^{23} cm^{-2} . These results from SMC X-1 and Centaurus X-3 suggest that high- η HMXBs exhibit considerably stronger spectral structures than ULXs, regardless of their accretion scheme (direct wind accretion or RLO).

4.6 New Possible Accretion Scenario in ULX

As described so far, the accretion mechanisms commonly seen in HMXB systems may have some difficulties in explaining the basic properties of ULX. This motivated us to look for a new accretion scenario.

4.6.1 Basic assumptions

In general, any explanation of ULXs, either sub-Eddington or super-Eddington, should be able to explain the following conditions.

- Sufficiently high mass accretion rates should be available, to generate the luminosity of $L_X = 10^{39\text{--}40} \text{ erg sec}^{-1}$.
- The accreting compact objects must have a considerable scatter in their masses, at least by an order of magnitude.
- Except the matter that accretes onto the central objects, the systems should be devoid of excess materials around them. Specially, the low and stable values of N_H and the upper limits on the Fe-K line EW should be explained.

Among these conditions, the second one strongly suggests that ULXs are BHs that are considerably more massive than the ordinary stellar-mass ones. Although the existence of such BHs used to be unclear, the 10 epic gravitational wave events detected with LIGO and Virgo (section 1), have finally revealed that such BHs as $\sim 50\text{--}80 M_\odot$ do exist, and are probably more abundant than was previously thought. Furthermore, such BHs can grow heavier through repeated mergers.

Although most of the ULX studies have so far implicitly assumed them as mass-exchanging binaries, the third condition above casts doubt on the presence of mass-donating

companion stars, particularly massive ones which are suggested by the ULX environment. Given these, we revive the idea of [Mii & Totani \(2005\)](#), who interpreted ULXs as single IMBHs, accreting directly via Bondi-Hoyle mechanism from dense parts of the interstellar medium (ISM). This scenario agrees with the preferred locations of ULXs, i.e., arms of spiral galaxies. Furthermore, such a possibility is actually suggested by a recent radio observations by [Oka et al. \(2016\)](#), that a molecular cloud near Galactic center may be perturbed due to a passage of an isolated BH with a mass of $\sim 10^5 M_\odot$. Below, let us revisit the scenario of [Mii & Totani \(2005\)](#), considering several properties of ULXs including those found in the present study.

4.6.2 Luminosity

Along with the above consideration, let us assume a BH with a mass M , entering with a relative velocity v into an ISM cloud which has a mass density ρ . Since the BH captures the ISM within the Bondi radius $R_B = 2GM/v^2$, the mass accretion rate is described as

$$\dot{M} = \rho \pi R_B^2 v = \frac{4\pi G^2 M^2 \rho}{v^3}. \quad (9)$$

Using again the radiation efficiency ζ , equation (9) can be translated into the luminosity as

$$L = \zeta \dot{M} c^2 = \frac{4\pi G^2 M^2 c^2 \zeta \rho}{v^3}. \quad (10)$$

Further converting the mass density to the number density $n = \rho/\mu m_p$, where μ and m_p are the mean molecular weight and the proton mass, respectively, the luminosity can be expressed as

$$L = 4 \times 10^{40} \zeta_{0.1} M_{100}^2 n_{100} v_1^{-3} \text{ erg sec}^{-1}. \quad (11)$$

Here, we assumed $\mu = 0.13$, and normalized the relevant quantities as $\zeta_{0.1} \equiv \zeta/0.1$, $M_{100} \equiv M/(100 M_\odot)$, $n_{100} \equiv n/(100 \text{ cm}^{-3})$, and $v_1 \equiv v/(1 \text{ km s}^{-1})$. Therefore, if a $100 M_\odot$ BH is drifting into an ISM cloud of $n \sim 100 \text{ cm}^{-3}$, with a relatively low velocity of $v \sim 1 \text{ km s}^{-1}$ ([Nakamura et al. 2016](#)), we expect $L \sim 4 \times 10^{40} \text{ erg sec}^{-1}$, which is high enough to explain ULXs.

The most important point of this Bondi-Hoyle scenario is the scaling of $L \propto M^2 v^{-3}$ in equation (10). The mechanism therefore works predominantly for rather massive BHs (as required by the second condition), because of the M^2 factor, as well as relatively lower values of v which more massive objects would acquire through dynamical friction ([Mii & Totani 2005](#); [Nakamura et al. 2016](#)).

4.6.3 Absorption and Fe-K lines

Below, the present scenario is tested against other observational facts. Let us first assume that a ULX is located at the center of an ISM cloud which has a linear size of $R_{\text{ISM}} = 3 \times R_3$ pc. Then, the absorption through the cloud will be

$$N_{\text{H}} \sim n R_{\text{ISM}} \sim 1 \times 10^{21} n_{100} R_3 \text{ cm}^{-2}. \quad (12)$$

Assuming $n_{100} \sim 1$ and $R_3 \sim 1$, this agrees with the low and stable absorption observed from the present ULX sample. For reference, the Bondi radius is $R_B = 0.9 M_{100} / v_1^2$ pc,

which is smaller than R_{ISM} , and the assumed ISM cloud has a mass of

$$M_{\text{ISM}} \sim \frac{4\pi}{3} R_{\text{ISM}}^3 \rho = 300 R_3^3 n_{100} M_\odot. \quad (13)$$

Next, we consider the fluorescent Fe-K lines, assuming that the cloud is spherically symmetric, and is illuminated by X-rays from the BH at its center. In this case, the Fe-K line EW is expected to be approximately proportional to N_{H} , as indicated by the dashed line in figure 8. Thus, when the cloud has $N_{\text{H}} \sim 10^{21} \text{ cm}^{-2}$, the Fe-K line EW will be several eV to $\sim 10 \text{ eV}$, which is fully consistent with the observed upper limits. This estimate is valid even when the matter within R_B is gradually accelerated inwards, as long as the flow can be approximated as spherically symmetric. The Doppler effect associated with the flow motion would rather reduce the EW of *narrow* lines, and would make the scenario even more favorable.

4.6.4 Activity duration

Finally, we evaluate two times scales involved in the proposed scenario. One is the crossing time of the BH through the ISM cloud, expressed as

$$\tau_1 = 2R_{\text{ISM}}/v = 3 \times 10^6 R_3/v_1 \text{ yr}. \quad (14)$$

The other is the time scale over which the mass accretion can be sustained. From equation (9) and equation (13), this can be derived as

$$\tau_2 = M_{\text{ISM}}/\dot{M} = \frac{(v R_{\text{ISM}})^3}{3G^2 M^2} = 5 \times 10^6 (v_1 R_3)^3 / M_{100}^2 \text{ yr}. \quad (15)$$

Thus, a single encounter between a massive BH and an ISM clump is estimated to have an activity duration as $\tau_1 \sim \tau_2 \sim$ a few million years. As already argued by [Mii & Totani \(2005\)](#), this time scale is sufficient to power the optical emission-line nebular seen around some ULXs.

As shown so far, the proposed scenario can consistently explain the three conditions raised in section 4.6.1. However, it still remains to be evaluated whether the number of such BHs (with a large uncertainty) and the volume filling factor of rather dense ISM clouds are both high enough to explain the average number of ULXs in each galaxy. It is also urgent to observationally examine whether ULXs are indeed imbedded in ISM clumps. These are left for our future study.

4.7 Possible accretion regime of ULX

Although we have so far discussed the possible mass distribution and the accretion mechanism of ULXs, their actual mass accretion regimes, in terms of η , are still left open to be examined. Therefore, let us finally conduct this attempt by referring to the knowledge of BHBs. As mentioned in section 4.3, BHBs are known to exhibit distinct spectral states as a function of η . Among several different ways of classification, we adopt that of [Kubota & Makishima \(2004\)](#), who identified, in the transient BHB XTE J1550-564, four major spectral states; the Low/Hard state (LHS; $\eta < 0.01$), the High/Soft state (HSS; $\eta \sim 0.1$), the Very High State (VHS; $\eta \sim 0.3$), and the Slim Disk State (SDS; $\eta \sim 1$). While [Kubota & Makishima \(2004\)](#) assigned the SDS literally to the state wherein the accreting matter forms a ‘‘slim disk’’

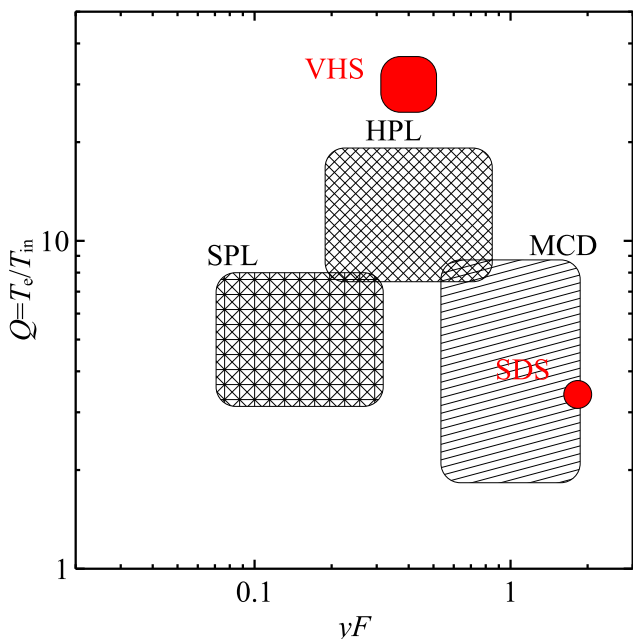


Figure 9. Typical locations of the spectral states of ULXs (black) and BHBs (red), on the yF vs. Q plane. See text for details.

(Abramowicz et al. 1988; Watarai et al. 2000), the spectra in this state can be reproduced alternatively, as touched in section 3.2.1, in terms of Comptonization, wherein the disk photons get Comptonized by a cool and optically-thick ($\tau \sim 10$) corona (e.g., Miyawaki et al. 2009; Middleton et al. 2011). In the present discussion, we adapt this interpretation of the SDS.

Since the spectra of ULX, all significantly Comptonized, were successfully characterized by Q and yF , we compare these parameters with those of the individual states of BHB, to seek for any common characteristics between the two classes of objects. Hereafter, we exclude the HSS and LHS of BHBs from our discussion, because the former shows no clear sign of thermal Comptonization, and the latter is known to exhibit $T_e \sim 100$ keV (e.g., Makishima et al. 2008) which much exceeds those of ULXs ($T_e \sim 2$ keV). In addition, the values of η in the LHS would be too low to explain ULXs. Figure 9 presents, on the (yF , Q) plane, rough locations of these spectral states of ULXs and BHBs. As detailed below, the parameters of BHBs were calculated or estimated utilizing results from several previous studies, including Done & Kubota (2006), Tamura et al. (2012), and Hori et al. (2014) for the VHS, as well as Kubota & Makishima (2004) for the SDS. Using this figure, let us attempt to find possible correspondence between BHBs and ULXs in terms of their spectral states.

Since few reports have so far been made on Comptonization modeling of BHB spectra in the SDS, we simulated a typical SDS spectrum of XTE J1550-564 obtained by Kubota & Makishima (2004), and fitted it with the present MCD+THC model, to obtain (yF , Q) \sim (2, 3). Therefore, on the (yF , Q) plane, the SDS spectra of BHBs occupy a very similar region to the MCD state of ULX. This agreement is very understandable, because these two states are both

characterized by strongly convex spectra. From these similarities, the MCD state of ULXs can be securely regarded as a spectral state corresponding to the SDS of BHBs, when the latter is considered to harbor Comptonized disks rather than slim disks. Then, like the SDS, the MCD state is implied to have $\eta \sim 1$. This implication is fully consistent with our interpretation of ULXs as BHs that are more massive than the ordinary stellar-mass BHs, because the maximum luminosity observed in the present ULX sample, $\sim 10^{40}$ erg sec^{-1} , is close to L_{edd} of $\sim 100 M_{\odot}$ BHs.

The Compton continuum of VHS is typically soft as $\Gamma = 2.3 - 2.6$ and rolls over at ~ 40 keV, which yield $T_e \sim 20$ keV and $y = 0.5 - 0.7$. At the same time, the VHS spectra show a strong soft excess component peaking at ~ 2 keV, which is considered as the directly visible accretion-disk emission, with $T_{\text{in}} \sim 0.5$ keV and $F = 0.6 - 0.8$. As a result, the VHS spectra are located typically at (yF , Q) \sim (0.4, 30). Thus, the yF values of the VHS fall on a range similar to those of the SPL and HPL of ULXs, although the values of Q are rather different. Since they have similar values of yF in figure 9, and similar continuum slopes ($\Gamma \sim 2.3 - 2.6$ of the VHS vs. $\Gamma \sim 2.4$ of the SPL state), we may assign the SPL state of ULXs to the VHS of BHBs. In addition, the SPL luminosities, which are 5 – 10 times lower than that of the MCD state (figure 7 D), is in a broad agreement with the values of $\eta \sim 0.3$ found in the VHS.

As described above, the SPL state of ULXs exhibited several times lower Q than those in the VHS of BHBs, and the difference could be attributed to the BH mass difference. In fact, when evaluated at the same η and the same distance scaled by the Schwarzschild radius, i.e., at the same intensity to be observed, the coronal electron density n_e should be inversely proportional to the BH mass if the accretion flow is radially self similar. Therefore, towards more massive systems, the Compton cooling of coronal electrons (with a rate $\propto n_e$) would dominate their Coulomb heating by hot ions ($\propto n_e^2$), resulting in a lower value of $Q = T_e/T_{\text{in}}$. As supporting evidence, the “soft excess” structures seen in active galactic nuclei have recently been described successfully as thermal Comptonization in coronae with even lower temperature as $T_e = 0.2 - 0.5$ keV (e.g., Noda et al. 2011; Done et al. 2012; Jin et al. 2016), although these massive BHs should have much lower η .

Our final issue is how to interpret the HPL state, wherein the Comptonization is further enhanced from the SPL state (Kobayashi et al. 2017). From the above two assignments, it is natural to consider that the HPL state is a new spectral state (possibly with $0.4 < \eta < 1$), which would fall, in BHBs, between the VHS and SDS. Although it is unclear at present why the corresponding state is not clearly observed from BHBs, an interesting observation was reported by Hu et al. (2018); they found that an extragalactic X-ray transient, called NGC 7793 P9, evolved from a presumably HSS of BHBs, into the SPL state, and further into the HPL and MCD states of ULXs. It is possible that the spectral state sequence of accreting BHs is not completely determined by η , but depends to some extent on the BH mass itself.

ACKNOWLEDGEMENTS

The authors would like to thank all the members of the *Suzaku*, *XMM-Newton*, and *NuSTAR* teams for their devotion to instrumental developments, calibration, and spacecraft operation. This present research has been financed by JSPS KAKENHI Grant Number JP 18H05873.

REFERENCES

- Abbott B. P., et al., 2016a, *Phys. Rev. Lett.*, 116, 061102
 Abbott B. P., et al., 2016b, *Phys. Rev. Lett.*, 116, 241103
 Abbott B. P., et al., 2017a, *Physical Review Letters*, 118, 221101
 Abbott B. P., et al., 2017b, *Phys. Rev. Lett.*, 119, 141101
 Abramowicz M. A., Czerny B., Lasota J. P., Szuszkiewicz E., 1988, *ApJ*, 332, 646
 Bachetti M., et al., 2013, *ApJ*, 778, 163
 Bachetti M., et al., 2014, *Nature*, 514, 202
 Barré H., Nye H., Janin G., 1999, *ESA Bulletin*, 100, 15
 Belczynski K., Bulik T., Fryer C. L., Ruiter A., Valsecchi F., Vink J. S., Hurley J. R., 2010, *The Astrophysical Journal*, 714, 1217
 Brightman M., et al., 2016, *ApJ*, 816, 60
 Carpano S., Haberl F., Maitra C., Vasilopoulos G., 2018, *MNRAS*, 476, L45
 Dickey J. M., Lockman F. J., 1990, *ARA&A*, 28, 215
 Done C., Kubota A., 2006, *MNRAS*, 371, 1216
 Done C., Davis S. W., Jin C., Blaes O., Ward M., 2012, *MNRAS*, 420, 1848
 Fabbiano G., Trinchieri G., 1987, *ApJ*, 315, 46
 Feng H., Kaaret P., 2006, *ApJ*, 650, L75
 Fürst F., et al., 2016, *ApJ*, 831, L14
 Gladstone J. C., Roberts T. P., Done C., 2009, *MNRAS*, 397, 1836
 Hagino K., Odaka H., Done C., Tomaru R., Watanabe S., Takahashi T., 2016, *MNRAS*, 461, 3954
 Harrison F. A., et al., 2013, *ApJ*, 770, 103
 Heida M., et al., 2015, *MNRAS*, 453, 3510
 Hori T., et al., 2014, *ApJ*, 796, 146
 Hu C.-P., Chou Y., Yang T.-C., Su Y.-H., 2013, *ApJ*, 773, 58
 Hu C.-P., Kong A. K. H., Ng C.-Y., Li K. L., 2018, preprint, ([arXiv:1808.07716](https://arxiv.org/abs/1808.07716))
 Inoue H., 1985, *Space Science Reviews*, 40, 317
 Israel G. L., et al., 2017a, *Science*, 355, 817
 Israel G. L., et al., 2017b, *MNRAS*, 466, L48
 Jin C., Done C., Ward M., 2016, *MNRAS*, 455, 691
 Kajava J. J. E., Poutanen J., 2009, *MNRAS*, 398, 1450
 Kajava J. J. E., Poutanen J., Farrell S. A., Grisé F., Kaaret P., 2012, *MNRAS*, 422, 990
 Kawashima T., Ohsuga K., Mineshige S., Yoshida T., Heinzeller D., Matsumoto R., 2012, *ApJ*, 752, 18
 King A. R., Davies M. B., Ward M. J., Fabbiano G., Elvis M., 2001, *The Astrophysical Journal Letters*, 552, L109
 Kitaguchi T., et al., 2014, in *Space Telescopes and Instrumentation 2014: Ultraviolet to Gamma Ray*. p. 91441R, doi:10.1117/12.2057342
 Kobayashi S., Nakazawa K., Makishima K., 2016, *Astronomische Nachrichten*, 337, 479
 Kobayashi S. B., Nakazawa K., Makishima K., 2017, *PASJ*, 69, 4
 Koyama K., et al., 2007, *PASJ*, 59, 23
 Kubota A., Makishima K., 2004, *ApJ*, 601, 428
 Makishima K., Maejima Y., Mitsuda K., Bradt H. V., Remillard R. A., Tuohy I. R., Hoshi R., Nakagawa M., 1986, *ApJ*, 308, 635
 Makishima K., et al., 2000, *ApJ*, 535, 632
 Makishima K., et al., 2008, *PASJ*, 60, 585
 Middleton M. J., Sutton A. D., Roberts T. P., 2011, *MNRAS*, 417, 464
 Middleton M. J., Walton D. J., Roberts T. P., Heil L., 2014, *MNRAS*, 438, L51
 Mii H., Totani T., 2005, *ApJ*, 628, 873
 Miller J. M., et al., 2006, *ApJ*, 646, 394
 Miller J. M., et al., 2012, *ApJ*, 759, L6
 Mineshige S., Ohsuga K., 2007, in Ho L. C., Wang J.-W., eds, *Astronomical Society of the Pacific Conference Series Vol. 373, The Central Engine of Active Galactic Nuclei*. p. 85
 Mitsuda K., et al., 1984, *PASJ*, 36, 741
 Mitsuda K., et al., 2007, *PASJ*, 59, S1
 Miyawaki R., Makishima K., Yamada S., Gandhi P., Mizuno T., Kubota A., Tsuru T. G., Matsumoto H., 2009, *PASJ*, 61, S263
 Mizuno T., et al., 2007, *PASJ*, 59, 257
 Motch C., Pakull M. W., Soria R., Grisé F., Pietrzyński G., 2014, *Nature*, 514, 198
 Naik S., Paul B., 2004, *A&A*, 418, 655
 Naik S., Paul B., Ali Z., 2011, *ApJ*, 737, 79
 Nakamura T., Nakano H., Tanaka T., 2016, *Phys. Rev. D*, 93, 044048
 Neilsen J., Hickox R. C., Vrtilik S. D., 2004, *ApJ*, 616, L135
 Noda H., Makishima K., Yamada S., Torii S., Sakurai S., Nakazawa K., 2011, *PASJ*, 63, S925
 Noda H., Makishima K., Yamada S., Nakazawa K., Sakurai S., Miyake K., 2014, *ApJ*, 794, 2
 Nowak M. A., Wilms J., Heindl W. A., Pottschmidt K., Dove J. B., Begelman M. C., 2001, *MNRAS*, 320, 316
 Oka T., Mizuno R., Miura K., Takekawa S., 2016, *ApJ*, 816, L7
 Orosz J. A., Steiner J. F., McClintock J. E., Buxton M. M., Bailyn C. D., Steeghs D., Guberman A., Torres M. A. P., 2014, *ApJ*, 794, 154
 Özel F., Saultis D., Narayan R., McClintock J. E., 2010, *ApJ*, 725, 1918
 Pinto C., Middleton M. J., Fabian A. C., 2016, *Nature*, 533, 64
 Pintore F., Zampieri L., 2012, *MNRAS*, 420, 1107
 Pintore F., Zampieri L., Stella L., Wolter A., Mereghetti S., Israel G. L., 2017, *ApJ*, 836, 113
 Ponti G., Fender R. P., Begelman M. C., Dunn R. J. H., Neilsen J., Coriat M., 2012, *MNRAS*, 422, L11
 Rappaport S. A., Podsiadlowski P., Pfahl E., 2005, *MNRAS*, 356, 401
 Remillard R. A., McClintock J. E., 2006, *ARA&A*, 44, 49
 Sakurai S., et al., 2014, *PASJ*, 66, 10
 Sasano M., 2015, *X-ray Studies of Highly Magnetized Neutron Stars in Binary Systems with Suzaku*
 Sathyaprakash R., et al., 2019, *MNRAS*, p. L104
 Savonije G. J., 1979, *A&A*, 71, 352
 Shakura N. I., Sunyaev R. A., 1973, *A&A*, 24, 337
 Shidatsu M., Done C., Ueda Y., 2016, *ApJ*, 823, 159
 Soria R., Wu K., Page M. J., Sakellou I., 2001, *A&A*, 365, L273
 Strüder L., et al., 2001, *A&A*, 365, L18
 Sunyaev R. A., Titarchuk L. G., 1980, *A&A*, 86, 121
 Sutton A. D., Roberts T. P., Middleton M. J., 2013, *MNRAS*, 435, 1758
 Takahashi T., et al., 2007, *PASJ*, 59, 35
 Tamura M., Kubota A., Yamada S., Done C., Kolehmainen M., Ueda Y., Torii S., 2012, *ApJ*, 753, 65
 The LIGO Scientific Collaboration et al., 2018, arXiv e-prints, Tombesi F., Cappi M., Reeves J. N., Palumbo G. G. C., Yaqoob T., Braito V., Dadina M., 2010, *A&A*, 521, A57
 Turner M. J. L., et al., 2001, *A&A*, 365, L27
 Vrtilik S. D., Raymond J. C., Boroson B., McCray R., 2005, *ApJ*, 626, 307
 Walton D. J., Miller J. M., Harrison F. A., Fabian A. C., Roberts T. P., Middleton M. J., Reis R. C., 2013, *ApJ*, 773, L9
 Walton D. J., et al., 2016, *ApJ*, 826, L26
 Watarai K.-y., Fukue J., Takeuchi M., Mineshige S., 2000, *PASJ*, 52, 133
 Wilms J., Allen A., McCray R., 2000, *ApJ*, 542, 914

Wilms J., Nowak M. A., Pottschmidt K., Heindl W. A., Dove J. B., Begelman M. C., 2001, *MNRAS*, **320**, 327
 Yamada S., et al., 2013, *ApJ*, **767**, L35
 Zdziarski A. A., Johnson W. N., Magdziarz P., 1996, *MNRAS*, **283**, 193
 Zhang Z., Sakurai S., Makishima K., Nakazawa K., Ono K., Yamada S., Xu H., 2016, *ApJ*, **823**, 131
 Życki P. T., Done C., Smith D. A., 1999, *MNRAS*, **309**, 561

This paper has been typeset from a $\text{\TeX}/\text{\LaTeX}$ file prepared by the author.

APPENDIX A: MODIFICATION TO THE SPECTRAL MODEL

As described in section 3.2.2, several MCD spectra in the present sample, one from IC 342 X-1 on 2004 February 20, and a few from NGC 1313 X-1 (table 3), should unnaturally low T_{in} , and yielded extremely large values of R_{in} . In this Appendix, we describe how these cases were treated by applying some modification to our canonical MCD+THC model.

Among the 7 spectra of IC 342 X-1, the one obtained on 2004 February 20 exhibited the anomaly (table 3). This particular spectrum, at the same time, required a stronger absorption of $N_{\text{H}} = 7.3 \times 10^{21} \text{ cm}^{-2}$ than that of 2005 February 10 ($N_{\text{H}} = 2.3 \times 10^{21} \text{ cm}^{-2}$), even though these two spectra have nearly identical shapes, as seen in figure 3 (E). We hence considered that the large R_{in} of the 2004 spectrum is an artifact caused by this apparently high absorption, and refitted the spectrum with the column density fixed to the average value ($N_{\text{H}} = 2.5 \times 10^{21} \text{ cm}^{-2}$) obtained from the other data sets. As shown in table 3, the fit slightly worsened, but T_{in} became higher ($T_{\text{in}} = 0.5 \text{ keV}$) than in the previous fit ($T_{\text{in}} = 0.16 \text{ keV}$). The revised value is consistent with that of 2005 ($T_{\text{in}} = 0.6 \text{ keV}$) and that of the MCD states seen in the other sources.

Among the 18 spectra of NGC 1313 X-1, 5 (e.g., 2014 May 27) implied the presence of a large disk. However, unlike the case of IC 342 X-1, these spectra showed similar N_{H} to those obtained in the other observations of this object. We considered that, these spectra actually harbor an extra soft component at 0.3–0.8 keV, and interpret it as emission from the outer part of the accretion disk, where the hot corona is no longer present and hence blackbody photons from this region reach us without upscattered. In order to represent this consideration, we modified our modeling by adding an extra `diskbb` model which represents this outer-disk (cool) emission, and let the original `diskbb+nthcomp` component to represent the inner-disk (hotter) region where the photons are Comptonized by the corona. The results utilizing this modified model are also shown in table 3 as additions to the original results. This modified model have actually improved the fits (table 3), and brought the inner-disk temperature ($T_{\text{in}2}$ in table 3) to 0.6–0.9 keV, which is consistent with those of the other MCD-state spectra in our sample. Furthermore, the parameters of the outer-disk ($T_{\text{in}1}$ and $R_{\text{in}1}$ in table 3) and those of the inner-disk ($T_{\text{in}2}$, $R_{\text{in}2}$) satisfy the temperature vs radius relation expected in the standard accretion physics ($T \propto r^{-0.75}$), where T is the effective temperature of the accretion disk, and r is the radius from the disk center; (Shakura & Sunyaev 1973).